ENG. Struct. Civ. Eng. 2026, 20(4): 804–827
https://doi.org/10.1007/s11709-026-1283-y

RESEARCH ARTICLE

Nonlinear mechanical behavior and shell-joint modeling method in rectangular pipe-jacking tunnel joints

Zhengdong HUANG[a,b,c], Youjun XU[b,c*], Pengfei LI[a], Chao ZHANG[b,c], Yuhan SHAN[a], Xu ZHANG[b,c]

[a] *Key Laboratory of Urban Security and Disaster Engineering, Ministry of Education, Beijing University of Technology, Beijing 100124, China*

[b] *School of Civil Engineering, Inner Mongolia University of Science and Technology, Baotou 014010, China*

[c] *Research Center of Urban Underground Engineering at Universities of Inner Mongolia, Baotou 014010, China*

[*] *Corresponding author. E-mail: xyoujun@163.com*

ABSTRACT Rectangular pipe-jacking tunnels are highly prone to longitudinal deformation under the influence of adjacent engineering activities, uneven foundation settlement, and changes in surface loads. These problems may lead to structural damage at the joints of rectangular pipe-jacking tunnels, potentially triggering engineering disasters. In response to these situations, this paper experimentally studies the effects of different foundation conditions and steel sleeve ring design parameters on their shear stiffness and rotational stiffness. It reveals three stages of joint failure: gap closure, steel sleeve ring stress, and deformation failure. A three-dimensional refined numerical simulation method is adopted to study the deformation and failure characteristics of joints under different foundation strengths and steel sleeve ring design parameters, analyze the mechanical performance of the joints of rectangular pipe-jacking tunnels, and verify the reliability of the experimental results. Based on the experimental and numerical simulation results, considering the nonlinear characteristics of the joints of rectangular pipe-jacking tunnels, a shell-joint theoretical model is constructed. Precise simulation is achieved through the combination of 'rotation + shear' dynamic elements, and the stiffness matrix at the joints and the calculation method of mechanical elements are derived. The shell-joint theoretical model is used to compare and verify the results of the joint tests of rectangular pipe-jacking tunnels, confirming the accuracy and practicality of the shell-joint theoretical model.

KEYWORDS rectangular pipe-jacking, shell-joint mechanical model, foundation stiffness, longitudinal deformation

1 Introduction

Rectangular pipe-jacking tunnels possess advantages like a high utilization rate of the cross-section, shallow overburden, and minimal impact on the surrounding environment. They have been extensively employed in projects such as urban subway stations, subway entrance and exit passageways, utility tunnels, undercity tunnels, and pedestrian underpasses [1–5]. Rectangular pipe–jacking tunnels generally utilize F-type socket joints; nevertheless, the stiffness at these joint locations is considerably lower than the stiffness of the pipe segments themselves, rendering them a vulnerable link [4]. Underground engineering activities in certain cities frequently present safety risks of waterproofing failure and structural damage to the joints of rectangular pipe-jacking tunnels, and can even lead to excessive uneven deformation along the longitudinal axis of the tunnel, imperiling the operational safety of the tunnel [6–8].

Rectangular pipe-jacking tunnels, shield tunnels, and integrated pipe galleries all have numerous joints and are longitudinally discontinuous cylinders [9–12], so, it is possible to borrow research ideas from existing research on force deformation at the joints of shield tunnels and integrated pipe galleries to further investigate rectangular pipe-jacking tunnel joints. The prefabricated lining technology for drill and blast tunnels has many unresolved issues, so a novel secondary lining structure combining a prefabricated inverted arch with a cast-in-place one suitable for such tunnels is proposed by Kong

Article history: Received Jul 5, 2025; Accepted Nov 8, 2025

et al. [13], and its joint connection strength and construction feasibility are addressed through various means. Zhang and Zhao [14] delves into the damage mechanism of longitudinal joints under large deformation induced by non-uniform pressure loads through experiments and erects a finite element model to explore the influence of diverse factors on mechanical properties. Zhou et al. [15] carried out full-scale tests to analyze the effect of two diverse types of spheroidal graphite iron joint plates on the mechanical properties of segment joint stiffness and got specific failure modes and design requirements.

Zhu et al. [16] performed prototype tests to analyze the deformation and stress of the concrete lining and joint of a quasi-rectangular shield tunnel and revealed the damage characteristics. Liu et al. [17,18] used a prototype test to reveal the failure mechanism of the segment joint of a quasi-rectangular shield tunnel. Ding et al. [19] studied the mechanical behavior and deformation failure of shield tunnel segments and bolts under the combined action of axial force, bending moment, and shear through a prototype test. Salemi et al. [20] used a direct shear test to study the mechanical behavior of the longitudinal joint in the shield tunnel lining, and a clear relationship between the stiffness of the contact point and the normal stress of the contact position was proposed. Chen et al. [21] used numerical simulation to study the failure mechanism, convergence deformation, and structural stiffness of a shield tunnel lining. Dong et al. [22] studied the relationship between crack development, failure mode of deformation joints, shear load, and fault deformation of tunnel segments through experiments and numerical simulation.

In the study of F-type socket joints in rectangular pipe-jacking tunnels, despite the reference of research approaches from traditional circular pipe-jacking tunnel joints and shield tunnel ring joints, there are considerable differences in the forms of these two types of joints [23,24], and the related theories cannot be directly applied, moreover, there are substantial differences in various aspects between rectangular and circular pipe-jacking tunnels using F-type socket joints, thus, this paper considers the interaction between segments and the foundation, and conducts laboratory segment joint shear and bending tests to study the shear and bending mechanical properties of F-type socket joints in rectangular pipe-jacking tunnels, and proposes a three-dimensional shell-joint model considering the structural characteristics, which simulates the actual bending and shear displacement, establishing the stiffness matrix and calculation methods, and the shell-joint theoretical model is used to simulate the laboratory joint tests of rectangular pipe-jacking tunnels, verifying its accuracy and practicality, and the expected research results have great theoretical significance and practical engineering value for the design of joints in rectangular pipe-jacking tunnels.

2 Large-scale experiments

2.1 Rectangular pipe-jacking parameters

The experiment is based on a pedestrian underpass project of a station that utilizes a rectangular pipe-jacking tunnel, combined with the mechanical performance test methods of shield tunnel ring joints. The structural form, dimensions, and materials of the test specimens are designed and determined. The test specimens use F-type socket joints, with their detailed dimensions shown in Fig. 1. The cross-sectional dimensions of the test pipe segments are 1625 mm in length and 1075 mm in height, with the longitudinal width being taken as 1500 mm, as shown in Fig. 1. The concrete strength grade used for the pipe segments is C50. The longitudinal connection method uses F-type socket joints, with the steel sleeve made of a Q235 steel plate. The cross-sectional dimensions are 1625 mm in length and 1075 mm in height, and the width along the tunnel's longitudinal axis is 341 mm, located 150 mm from the socket end. The distance from the socket end to the spigot end is 191 mm. The gasket material is either chloroprene rubber or ethylene-propylene-diene rubber (EPDM). To facilitate the installation of the rectangular pipe-jacking segments and prevent the rubber gasket from being damaged due to excessive compression deformation, the middle portion of the thicker side of the original rubber gasket is removed to form the beak-shaped rubber gasket shown in Fig. 1. The initial height of the rubber gasket is 28 mm, the distance from the socket end is 80 mm, the rubber fixing groove depth, h, is 11.5 mm, and the installation clearance, d, is 4.5 mm. The initial compression height of the rubber gasket is 12 mm (28 – (11.5 + 4.5)). The reinforcing steel bars, stirrups, and structural steel bars are HRB400 steel bars. They are arranged in double layers on the inside and outside, except the stirrups, which are all Φ12. The thickness of the concrete cover is 30 mm, and the stirrups are Φ8@150. The test pipe segment is shown in Fig. 1.

2.2 Load and measurement system

Laboratory joint tests were separately carried out for joint shear tests and joint bending tests to investigate the relationships between shear force and relative shear deformation, moment and relative rotation angle, as well as the shear stiffness and rotational stiffness of the joints. To better observe the test phenomena, both the shear test and the bending test were loaded in a displacement-controlled manner. The loading regime was divided into a

total of 14 levels. Considering that the stress and deformation of the joints of the rectangular pipe-jacking tunnel are relatively small in the initial stage of loading and larger in the later stage, the increment of each of the first four levels was 5 mm. Starting from the fifth level, the increment of each level was 3 mm. The test was stopped when significant damage occurred to the joints. The servo-hydraulic jack used for test loading was equipped with a load sensor at the upper end. While performing displacement loading, the applied reaction force could also be obtained, so that the shear force and bending moment at the joints could be calculated. To explore the effects of diverse types of strata on the joints of rectangular pipe-jacking tunnels, for both the shear test and bending test, the design method of relative stiffness groups and absolute stiffness groups was utilized, leading to a total of 8 working conditions. The detailed information for each working condition is presented in Table 1. The relative stiffness group mainly focuses on examining the effects of gravel sand, silt, and clay strata on the joint stiffness under the two types of tests; while the absolute stiffness group highlights the influence of joint parameters on the joint stiffness under the two types of tests.

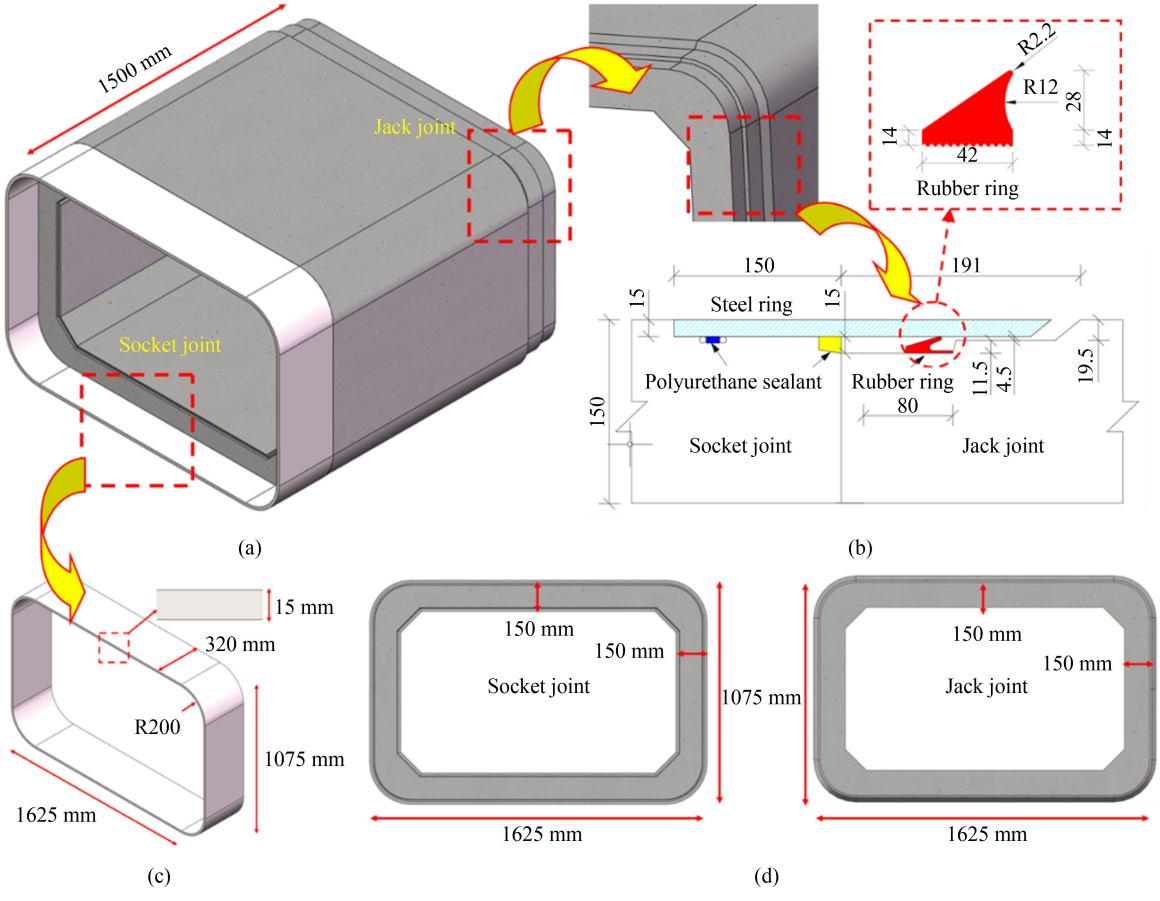

Fig. 1 Joint configuration: (a) rectangular pipe-jacking; (b) local structure for rectangular pipe-jacking; (c) steel ring; (d) socket and jack joint.

Table 1 Test working condition settings

Test name	Condition	Number of springs	Total stiffness (N/mm)	Foundation subgrade stiffness, K_v (kN·m^3)	Equivalent land strata
Laboratory joint shear test	Relative stiffness 1	9	15601	50	gravel sand
	Relative stiffness 2	6	10405	30	silt
	Relative stiffness 3	4	6943	15	clay strata
	Absolute stiffness	0	0	0	
Laboratory joint bending test	Relative stiffness 1	18	15601	50	gravel sand
	Relative stiffness 2	12	10405	30	silt
	Relative stiffness 3	8	6943	15	clay strata
	Absolute stiffness	0	0	0	–

After each loading stage, a 5-min stabilization period is maintained to observe the pipe section's deformation and fracture formation. The experiment was terminated when the joint sustained substantial damage. During the experiment of shearing, the two jacks use synchronized and equal displacement increases to conduct the joint's shear test to prevent large vertical displacement differences in the middle pipe section from causing bending deformation of the joint. The bending test was conducted via a single servo-hydraulic jack accompanied by a load distribution beam to attain uniform rotational deformation of the two pipe segments. Both the shear and bending tests made use of servo hydraulic jacks which were fitted with load sensors at the top. As loading was controlled by displacement, the applied reaction force could also be measured, facilitating the calculation of joint shear forces and moments. The experimental setup is shown in Fig. 2.

When carrying out the shear test, three pipe segments are initially assembled in the longitudinal direction and then pre-tightened to simulate the pipe-jacking process. To ensure the results under pure shear conditions, the ends of the pipe segments are fixed, and the middle segment is supported by the support system. Displacement sensors are symmetrically placed along the central axis of the tunnel for the shear test, with the layout of the sensors on one side of the pipe segment shown in Fig. 3(a). A total of 14 displacement sensors are positioned at the socket and spigot joints to measure the vertical, radial, and offset deformations of the pipe segments during loading.

When performing the bending test, the assembly process of the pipe segments is similar to that of the shear test, with two pipe segments assembled in the longitudinal direction and then pre-tightened. Both ends of the pipe segments are supported, and an allocation beam is

(a) (b)

Fig. 2 Laboratory joint test: (a) laboratory joint shear test; (b) laboratory joint bending test.

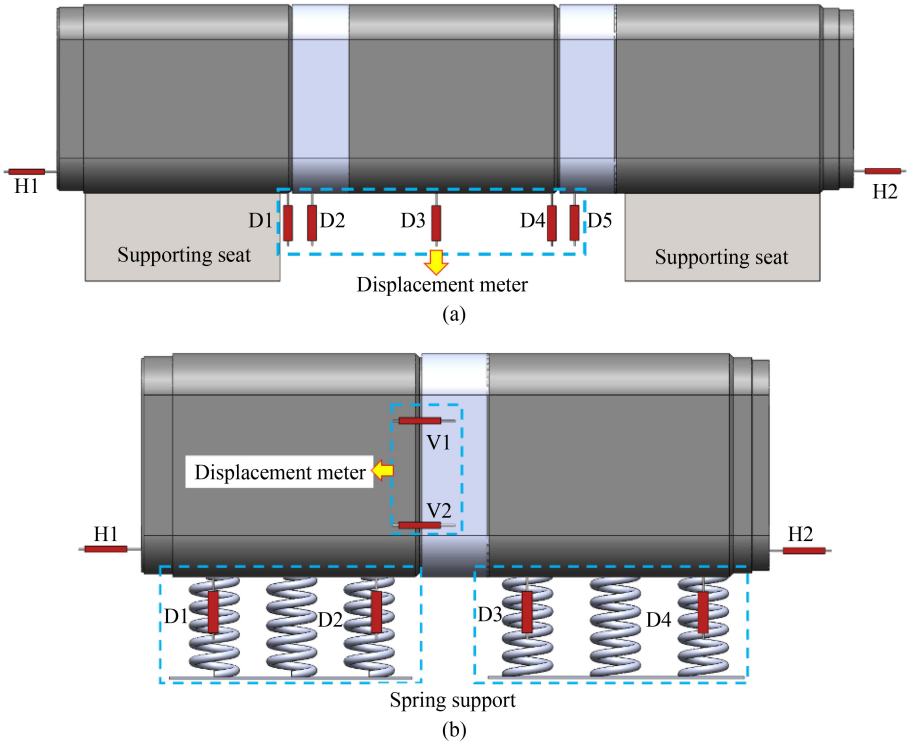

Fig. 3 Displacement sensor layout: (a) joint shear test; (b) joint bending test.

placed on the top of the pipe segments for vertical loading. Similar to the shear test, the displacement sensors are symmetrically arranged along the central axis of the tunnel for the bending test, with the layout of the sensors on one side of the pipe segment shown in Fig. 3(b). A total of 16 displacement sensors are positioned at the socket and spigot joints to measure the deflection and opening of the joints during loading. In Fig. 3, D1 to D4 are vertical displacement gauges, H1, and H2 are longitudinal displacement gauges, and V1 and V2 are opening displacement gauges.

To monitor internal crack initiation and propagation, 4 high-definition industrial cameras (model: Basler acA2040-90uc) were installed: 2 at the socket end and 2 at the spigot end of the joint. Key parameters of the cameras: resolution 2048 × 1536, frame rate 5 fps, lens focal length 16 mm. The cameras were aligned with the concrete chamfer and steel sleeve ring contact area, and synchronized with displacement sensors for data acquisition (sampling interval: 1 s), as shown Fig. 4.

2.3 Supporting system of stratum

To reflect the interaction between the stratum and the pipe segment and better simulate the true structural loading conditions, this experiment adopts a support system consisting of springs, cover plates, and spring supports placed under the loaded pipe segment. This system responds to the interaction between the elastic soil foundation and the superstructure in actual engineering. As shown in Fig. 5.

Fig. 4 Detail drawing of high-definition industrial camera: (a) front side; (b) back side.

The support system makes use of an equal distribution of equivalent foundation springs under the pipe segment to obtain vertical support from the stratum. There is a correlation between the number of equivalent foundation springs (k) and the value of the equivalent base subgrade stiffness (K_v), enabling the simulation of different stratum conditions by changing the number of equivalent foundation springs. The springs are arranged circumferentially around the rectangular pipe segment (1625 mm × 1500 mm), as shown in Fig. 5. According to the test conditions plan in Table 1, equivalent foundation springs are evenly arranged in different quantities to represent the pipe segments in different strata. In the shear test, when all 9 springs are deployed at the bottom of the pipe segment, it represents that the pipe segment is in gravel sand stratum at this time. Six springs and four springs represent that the pipe segment is in silty sand stratum and clay stratum respectively. Due to the principle that the foundation reaction produced by a unit displacement of the foundation is equal, the equivalent base subgrade stiffness (K_v) is expressed as:

$$K_v = \frac{nk}{S}, \tag{1}$$

where n is the number of equivalent foundation springs; k is the stiffness of a single equivalent foundation spring (1734 kN/m); nk is the total foundation stiffness of the equivalent foundation springs under the pipe segment; S is the area of the pipe segment bottom plate.

For the bending test, the deflection at the bottom of the pipe segment changes with deformation, so the calculation method consistent with that of the shear test cannot be used. According to the force balance $\sum M = 0$ of the pipe segment, the joint bending moment M can be obtained as shown in Fig. 6. Here, F is the load of the

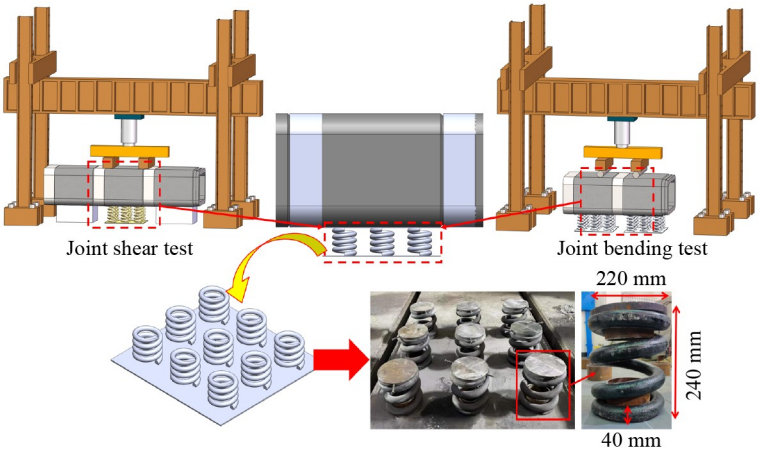

Fig. 5 Physical support system.

upper jack, which can be directly obtained from the sensor, and the ky_i (i = 1,2,3) is the reaction force of the equivalent foundation spring, the value of 'i' represents the number of springs at that position. where F_s is the joint shear force.

2.4 Experimental data analysis

2.4.1 Rectangular pipe-jacking displacement

By extracting the joint shear forces and segment misalignments from the shear test, the shear force-relative shear deformation curves for the joints under diverse working conditions in the shear test were acquired, as shown in Fig. 7.

From Fig. 7, it can be noticed that under diverse working conditions, the joints present different characteristics as the shear displacement goes up. This is chiefly because of some errors in the assembly of the test samples, and the failure points and failure times of the samples are not entirely the same. On the whole, the shear deformation of each joint can be divided into three phases based on the slope of the deformation curve.

Phase 1: Linear elastic deformation phase. At the outset of the test, the steel sleeve ring and the beak rubber at the socket joint gradually compress, and the various parts of the socket merely come into contact and are compressed. Due to the action of the steel sleeve ring, the concrete at the top corner of the socket end is the first to show alterations, with the emergence of multiple fine cracks, followed by a small bulge at the top of the steel sleeve ring. This process has the greatest slope and the highest shear stiffness.

Phase 2: Steel sleeve ring yield phase. The upper concrete of the pipe segment socket rapidly develops cracks, with a substantial increase in the number of cracks and the occurrence of crushing phenomena. The bulge at the top of the steel sleeve ring becomes more pronounced, and the chamfer of the steel sleeve ring undergoes a 'warping' phenomenon.

Phase 3: Concrete cracks at the chamfer rapidly expand outward, cracks appear on the side wall of the joint, and the concrete at the upper and chamfer areas of the socket end shows severe crushing. The chamfer of the steel sleeve ring yields and the displacement changes become slower. The joint enters the plastic stage, and ultimately, the steel sleeve ring undergoes shear failure.

Figure 8 presents the moment-relative rotation angle curves for the joints under diverse working conditions in the bending test. From Fig. 8, it can be noticed that the curve is divided into three phases based on the loading deformation:

Phase 1: When the bending test starts, the gap between the steel sleeve ring and the concrete at the joint gradually

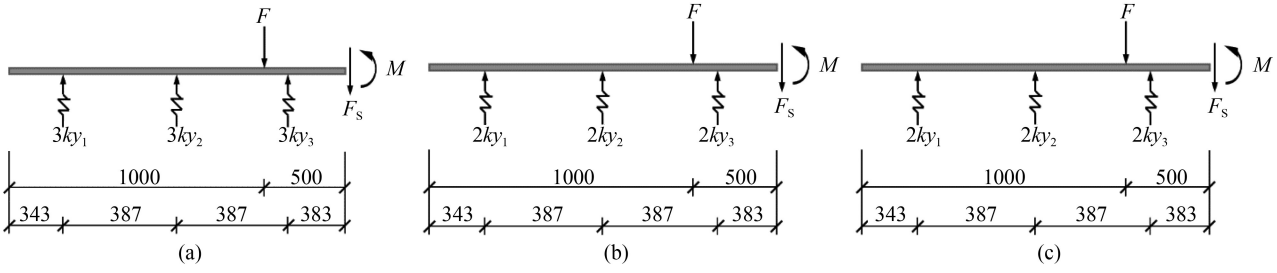

Fig. 6 Force diagram of pipe-jacking joint: (a) 9 springs; (b) 6 springs; (c) 4 springs.

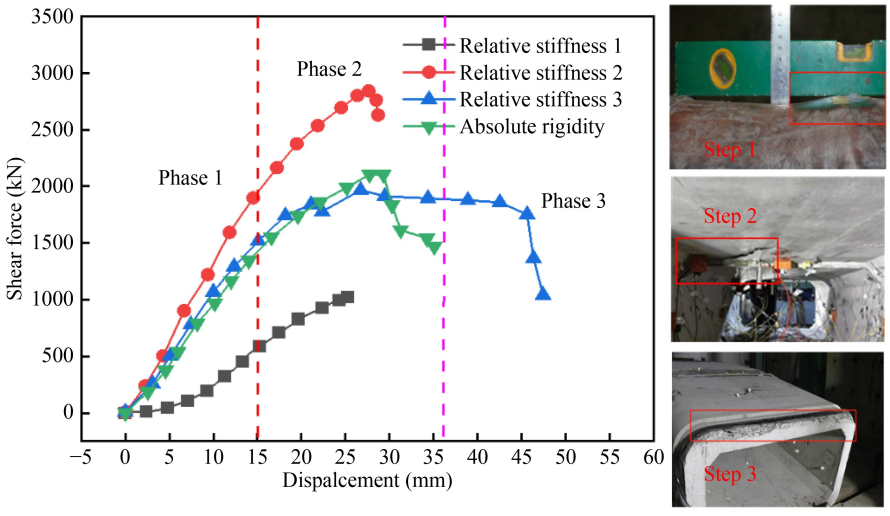

Fig. 7 Shear force-relative shear deformation curves for joints under different working conditions.

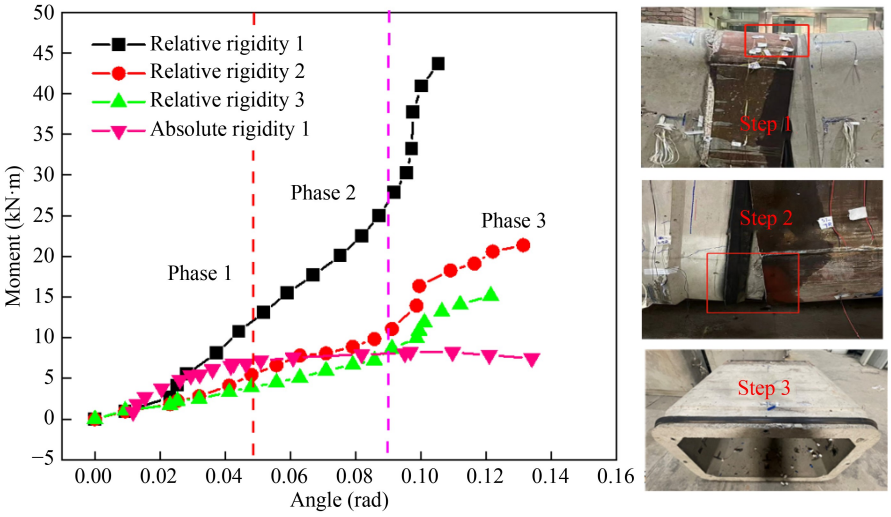

Fig. 8 Moment-relative rotation angle curves for joints under different working conditions.

decreases till they come into contact. Due to the downward rotational displacement of the spigot end, the top surface of the steel sleeve ring shows an upward deformation trend, and the bottom surface of the steel sleeve ring shows a downward deformation trend. During this process, stress concentration takes place at the four chamfer locations of the steel sleeve ring.

Phase 2: Small microcracks emerge in the top and bottom concrete of the spigot end of the pipe segment, and the steel sleeve ring is in close contact with the pipe segment. As the loading progresses, the cracks in the spigot end concrete rapidly develop, and the crack width increases. The top and bottom surfaces of the steel sleeve ring show slight warping phenomena. Under the action of the bending moment, the spigot end at the bottom of the pipe segment gradually slips out from the steel sleeve ring, and the steel sleeve ring first contacts the first-step concrete at the spigot. As the bending moment increases, the bottom continues to separate, and the steel sleeve ring compresses from the first-step concrete to the second-step concrete, at which point the steel sleeve ring undergoes slight deformation.

Phase 3: Eventually, due to multiple failures in the top and chamfer areas of the spigot end and the extension of cracks to the side wall, the side wall also produces a certain degree of damage. The warping of the steel sleeve ring is evident, and the steel sleeve ring separates from the second-step concrete. The steel sleeve ring experiences a rebound phenomenon, with some residual deformation, until the bottom of the pipe segment separates. At this time, due to excessive deformation, the structure of the pipe segment joint fails, and the test is terminated.

2.4.2 Rectangular pipe-jacking failure process

Figure 9 illustrates the deformation and failure of the steel sleeve ring and the joint concrete in the shear conditions. The primary damage to the steel sleeve ring is noticed as bulging at the chamfer and cracking at the weld. This takes place since the steel sleeve ring endures most of the shear force during the shear deformation of the joint. The concrete at the joint is continuously compressed as it resists the external loads, leading to stress concentration in the chamfer area, which makes the steel sleeve ring bulge in that region. In addition, the welding process lessens the edge strength of the material near the weld, resulting in the steel sleeve ring at the weld edge tearing apart under large deformations. Consequently, the weld ought not to be situated at the chamfer, and the steel sleeve ring at the chamfer should be locally reinforced.

As the shear load rises progressively, the contact pressure between the steel sleeve ring and the socket joint concrete keeps on increasing. Eventually, the steel ring is crushed near the contact surface of the concrete, and multiple diagonal cracks emerge in that area. With continuous loading, the upper load and the reaction force of the spring at the pipe bottom continue to compress the pipe segment, causing the pipe to collapse. The local diagonal cracks interconnect and develop. During the test, it can be observed that the cracks at the joint continuously expand and extend, accompanied by the concrete spalling off.

For the joint bending failure process, it can be divided into three stages based on the closing of the gap and the changing trends of force and deformation. Stage I: Gap Closing ($\theta \approx 0$–0.02 rad). The initial gap rapidly decreases from approximately 4.5 mm. The bending moment hardly increases with the rotation angle, and the elastic-plastic deformation of the concrete and the steel sleeve ring can be neglected. Stage II: Elastic Stage ($\theta \approx 0.02$–0.08 rad). The steel sleeve ring and the concrete achieve effective contact. The bending moment increases nearly linearly with the rotation angle. The contact pressure and contact area in the upper part (compression zone) steadily expand as the load increases. In the lower part (tensile zone), the

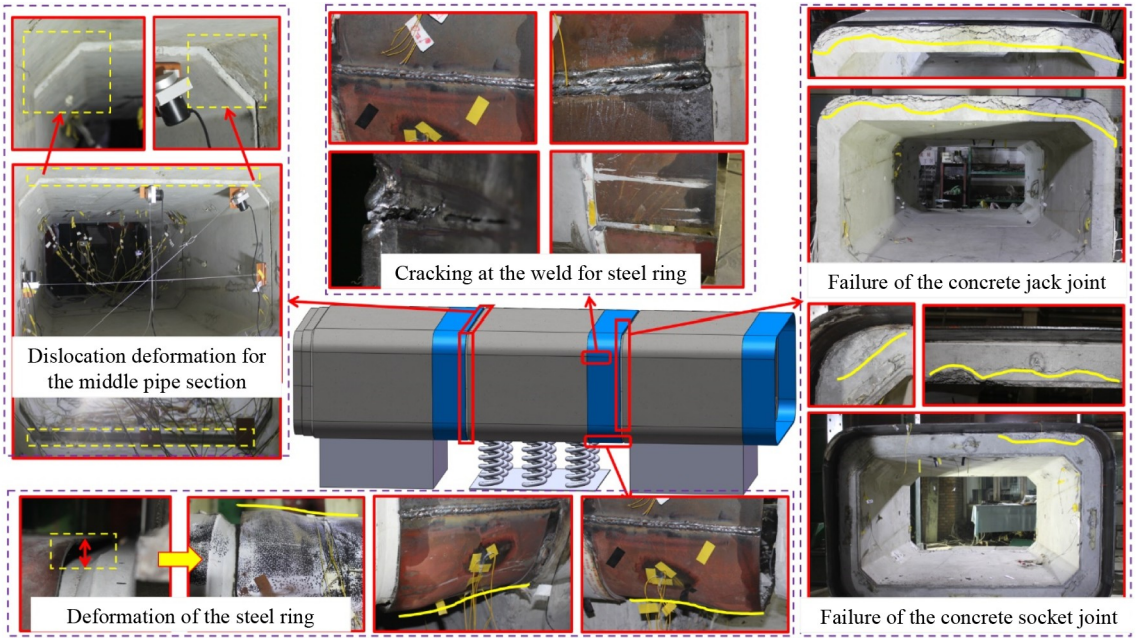

Fig. 9 Shear test failure phenomenon.

contact gradually weakens and shows a tendency to open, but the overall response is still controlled by elasticity, and no strength degradation occurs. Stage III: Deformation and Separation Stage (θ > 0.08 rad). The chamfer of the steel sleeve ring on the compressed side enters the yield state, and the compressed concrete fails. In the upper part, the plastic zone mainly characterized by crushing and yield bands develops in the concrete. In the lower part, the opening increases, and the spigot end gradually separates from the steel sleeve ring, accompanied by local springback and unrecoverable residual deformation. As the bottom opening becomes too large and the mechanical boundary conditions are lost, the overall bending bearing capacity of the structure fails, and the test is terminated. Under the overall bending action, the pipe segment shows a typical bending failure pattern of "compact upper part and open lower part", as shown Fig. 10.

3 Numerical simulations

3.1 Model size and material parameters

Considering the high cost of large-scale tests, this paper employs ABAQUS software to establish a three-

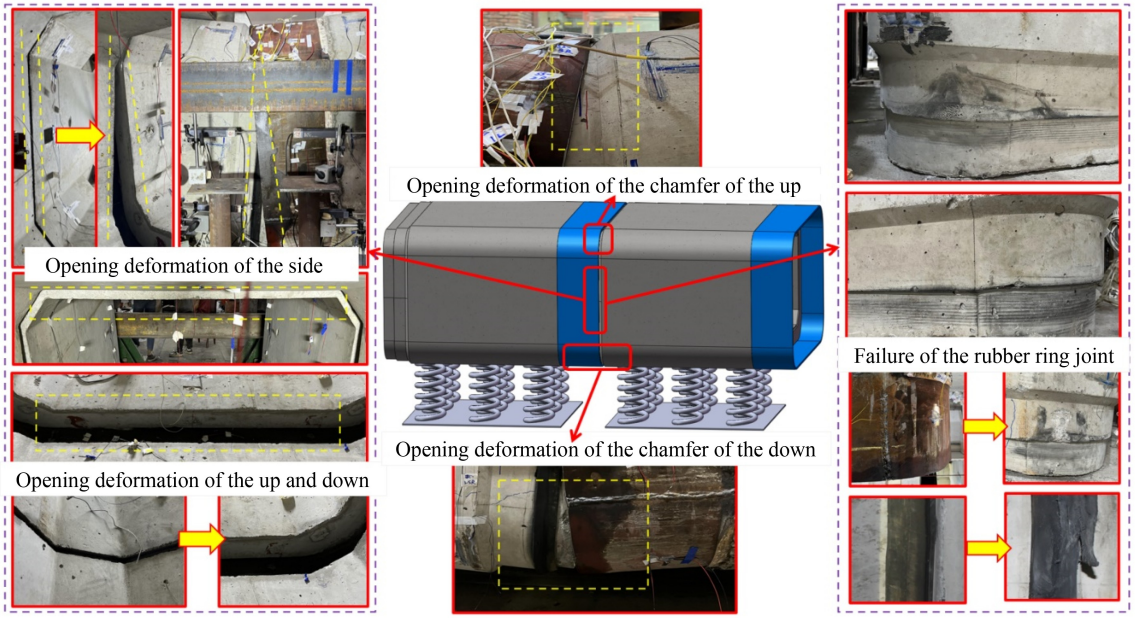

Fig. 10 Bending test failure phenomenon.

dimensional refined numerical model. Due to its high accuracy, the refined finite-element model can be used to complement the mechanism research of experiments (such as stress distribution and loss evolution). By altering the stiffness of different foundations, the failure characteristics of rectangular pipe-jacking joints are studied in detail. The model comprises two loading beams and reinforced concrete pipe-jacking, and the detailed dimensions and mesh division are shown in Fig. 11. The concrete has a strength grade of C50, and the steel cage is made of Q235 steel. The settings for loads and boundary conditions are the same as those in the experimental process. Vertical loads are applied by arranging two loading beams on the reaction frame, and simply supported constraints are set at the bottom of the assembled pipe joints to restrict the vertical displacement of the pipe joint bottom. Considering the computational efficiency and accuracy of the model, the mesh size is set at 50 mm.

In this paper, the elastic-plastic damage constitutive model is employed to simulate the mechanical properties of concrete. This model assumes that the uniaxial tensile and compressive responses of concrete are characterized by damaged plasticity. In the case of uniaxial tension, the stress–strain response follows a linear elastic relationship until failure. The failure stress corresponds to the occurrence of micro-cracks in the concrete material. Beyond the failure stress, the formula for micro-cracking adopts a softening stress–strain response to represent it macroscopically, leading to strain localization in concrete structures. In this simulation, the performance parameters of C50 concrete are presented in Table 2.

In ABAQUS, establishing the elastic-plastic damage constitutive model requires defining the compressive behavior (yield stress, inelastic strain, compression damage parameter, tensile recovery) and the tensile behavior (yield stress, inelastic strain, compression recovery). The stress-strain relationship of concrete under compression and its damage quantification parameters are as follows:

$$\sigma = (1 - d_c) E_c \varepsilon, \tag{2}$$

$$d_c = \begin{cases} 1 - \dfrac{\rho_c n}{n - 1 + x^n}, & x \leqslant 1, \\ 1 - \dfrac{\rho_c}{\alpha_c (x - 1)^2 + x}, & x > 1, \end{cases} \tag{3}$$

$$\rho_c = \frac{f_{c,r}}{E_c \varepsilon_{c,r}}, \tag{4}$$

$$n = \frac{E_c \varepsilon_{c,r}}{E_c \varepsilon_{c,r} - f_{c,r}}, \tag{5}$$

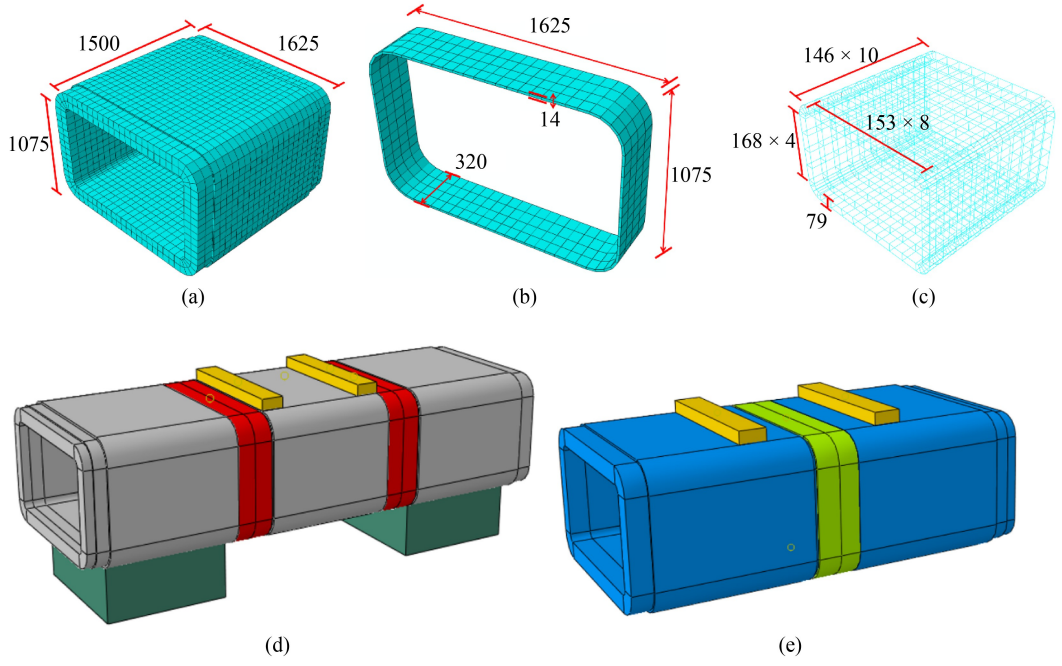

Fig. 11 Schematic diagram of mesh division for the main components of the model: (a) pipe mesh division diagram (unit: mm); (b) steel-ring mesh division diagram (unit: mm); (c) reinforcing cage mesh division diagram (unit: mm); (d) schematic diagram of the shear model; (e) schematic diagram of the bending model.

Table 2 C50 concrete performance parameters

Density (kg/m^3)	Young's modulus (MPa)	Poisson's ratio	Expansion angle (°)	Eccentric angle (°)	f_{b0}/f_{c0}	K	Viscosity parameter
2500	3450	0.2	32	0.1	1.16	0.6667	0.0005

$$x=\frac{\varepsilon}{\varepsilon_{c,r}}, \tag{6}$$

$$\varepsilon_{c,r}=\left(700+172\sqrt{f_c}\right)\times10^{-6}, \tag{7}$$

$$\alpha_c=0.157f_c^{0.785}-0.905, \tag{8}$$

$$\frac{\varepsilon_{cu}}{\varepsilon_{c,r}}=\frac{1}{2\alpha_c}(1+2\alpha_c+\sqrt{1+4\alpha_c}), \tag{9}$$

$$\varepsilon_c^{in}=\varepsilon_c-\varepsilon_{0c}^{el}, \tag{10}$$

$$\varepsilon_{0c}^{el}=\frac{\sigma_c}{E_0}, \tag{11}$$

$$\varepsilon_c^{pl}=\varepsilon_c^{in}-\frac{d}{(1-d)}\frac{\sigma_c}{E_0}, \tag{12}$$

$$d=1-\sqrt{\frac{\sigma}{E_0\varepsilon}}. \tag{13}$$

In the formula: α_c represents the parameter value of the descending segment of the stress–strain curve under the uniaxial compressive stress state of concrete; $f_{c,r}$ is the representative value of the uniaxial compressive strength of concrete; $\varepsilon_{c,r}$ is the peak compressive strain corresponding to $f_{c,r}$ the uniaxial compressive strength of concrete; d_c is the compressive damage evolution parameter of concrete, which represents the rule that the slope of the stress–strain curve of concrete continuously decreases after the loading starts; ε_c^{in} in is the compressive inelastic strain; ε_c is the actual strain of concrete; ε_{0c}^{el} is the elastic strain under the initial stiffness; ε_{0c}^{pl} is the compressive plastic strain; d is the concrete damage factor.

The concrete tensile stress−strain relationship and its damage quantification parameters are as follows:

$$\sigma=(1-d_t)E_c\varepsilon, \tag{14}$$

$$d_t=\begin{cases}1-\rho_t(1.2-0.2x^5), & x\leqslant 1,\\ 1-\dfrac{\rho_t}{\alpha_t(x-1)^{1.7}+x}, & x>1,\end{cases} \tag{15}$$

$$\rho_t=\frac{f_{t,r}}{E_c\varepsilon_{t,r}}, \tag{16}$$

$$x=\frac{\varepsilon}{\varepsilon_{t,r}}, \tag{17}$$

$$\varepsilon_{t,r}=f_{t,r}^{0.54}\times65\times10^{-6}, \tag{18}$$

$$\alpha_t=0.312f_{t,r}^2, \tag{19}$$

$$\varepsilon_t^{ck}=\varepsilon_t-\varepsilon_{0t}^{el}, \tag{20}$$

$$\varepsilon_{0t}^{el}=\frac{\sigma_t}{E_0}, \tag{21}$$

$$\varepsilon_t^{pl}=\varepsilon_t^{ck}-\frac{d}{(1-d)}\frac{\sigma_t}{E_0}. \tag{22}$$

In the formula: α_t represents the parameter value of the descending segment of the stress–strain curve under the uniaxial tensile stress state of concrete; $f_{t,r}$ is the representative value of the uniaxial tensile strength of concrete; $\varepsilon_{t,r}$ is the peak tensile strain corresponding to $f_{t,r}$ the uniaxial tensile strength of concrete; d_t is the tensile damage evolution parameter of concrete, which represents the rule that the slope of the stress–strain curve of concrete continuously decreases after the loading starts; ε_t^{ck} in is the tensile inelastic strain; ε_t is the actual strain of concrete; ε_{0t}^{el} is the elastic strain under the initial stiffness; ε_t^{pl} is the tensile plastic strain.

The stress–strain curves of concrete under uniaxial compression and tension are presented in Fig. 12.

The interaction between the various contact surfaces of the specimen is simulated by setting contact properties, which are mainly categorized into normal and tangential interactions. Normal interaction is defined as hard contact. Under this contact property, when the contact surfaces separate, the interface contact pressure becomes zero. When the interface gap is zero, the contact pressure can reach a certain value, and the sections are allowed to separate after contact. The tangential interaction is determined by penalty friction. In ABAQUS, friction is

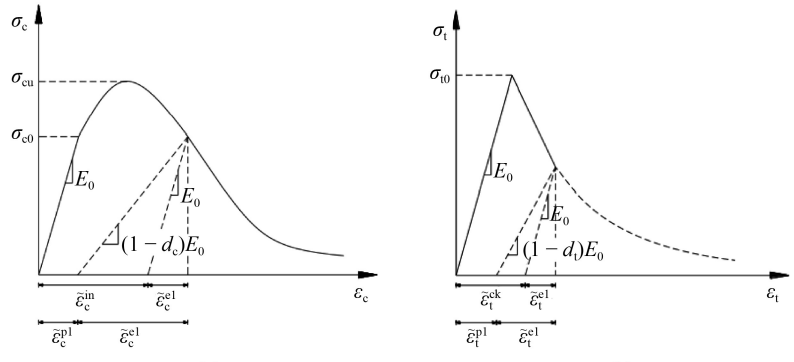

Fig. 12 Uniaxial compression and uniaxial tensile stress–strain curves: (a) uniaxial compressive stress–strain relationship; (b) uniaxial tensile stress–strain relationship.

calculated based on the classical Coulomb friction law, which indicates the maximum shear stress permitted for sliding between contact interfaces. By default, the friction coefficient is a fixed value, and the shear force is directly proportional to the friction coefficient. The friction stress can be expressed as $\tau_{cri} = \mu\sigma$, where μ, taken as 0.3, is the friction coefficient, and σ is the normal stress between the contact surfaces.

3.2 Numerical results and verification

3.2.1 Failure analysis of steel ring and pipe jack concrete of shearing test

The three-dimensional numerical simulation results present the stress distribution of the steel sleeve ring in an intuitive and refined way, as shown in Fig. 13. It can be observed that in the joint test results, only the failure of the steel sleeve ring at the chamfer can be seen. However, in the numerical simulation, stress concentration occurs at the chamfer (with a maximum stress of 235 MPa, reaching the yield strength of Q235 steel). This detail is difficult to observe in the test, providing an explanation at the mechanism level for the test phenomenon.

In the numerical simulation of the shear test, the deformation and failure trend of the steel sleeve ring is generally in line with the test. It can be noticed that the stress at the chamfer of the steel sleeve ring is notably higher than other parts, and the stress values gradually decrease from the chamfer to the side walls and the upper and lower surfaces. The main stress area of the left steel sleeve ring is at the bottom of the two chamfers, as that is where the steel sleeve ring is fixed with the left pipe segment joint as the socket. During the downward movement of the middle pipe segment, the bottom of the steel sleeve ring chamfer undergoes a significant compressive force, resulting in high stress at the chamfer. Regarding the right steel sleeve ring, the main stress area is at the upper two chamfers, as that is where the steel sleeve ring is fixed with the middle pipe segment joint as the socket. During the downward movement of the middle pipe segment, the top of the steel sleeve ring chamfer experiences a high-stress concentration due to the constraint from the right pipe segment, with a stress value reaching 235 MPa, which has reached the yield point.

It can be observed that in the numerical simulation, the degree of concrete damage is consistent with the stress distribution in the steel sleeve ring. However, due to the overall wrapping and pulling effect of the steel sleeve ring in the numerical simulation, the concrete damage range is wider than that in the experiment, extending from the chamfer to the side wall. This is because the numerical model assumes that there is no assembly gap between the steel sleeve ring and the concrete, while in the actual test specimens, there is a gap of 0.1–0.2 mm (due to assembly errors). This gap reduces the stress transfer in the test, thus limiting the damage. Secondly, micro - cracks will occur in the concrete specimens during the test, and these micro-cracks will locally disperse the stress, reducing the overall damage range. When comparing the results of the numerical simulation with those of the indoor joint test, the damage of the concrete is also generally consistent. The damage in the stress-concentrated area at the chamfer of the pipe segment joint is relatively large, as shown in Fig. 14.

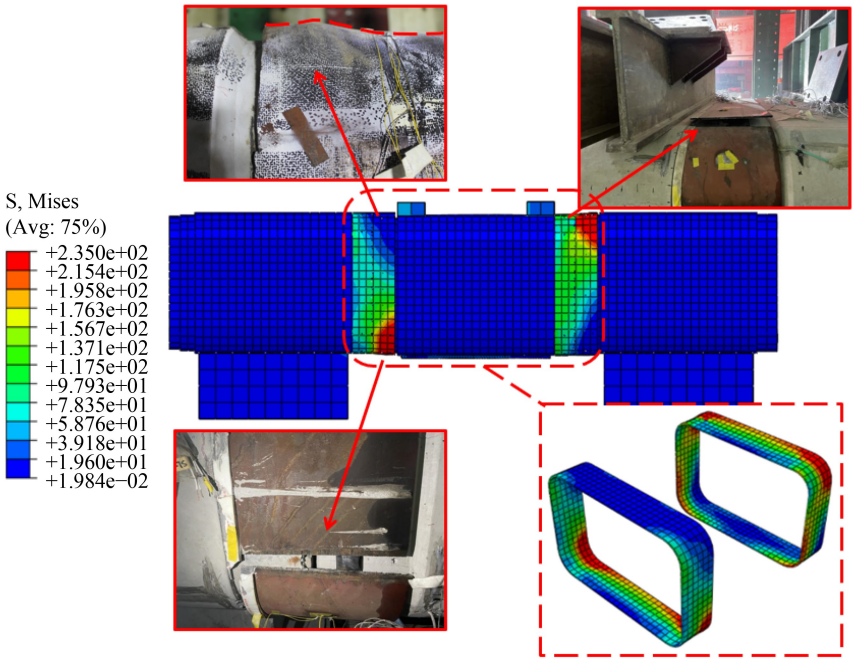

Fig. 13 Verification of numerical simulation results with experimental results.

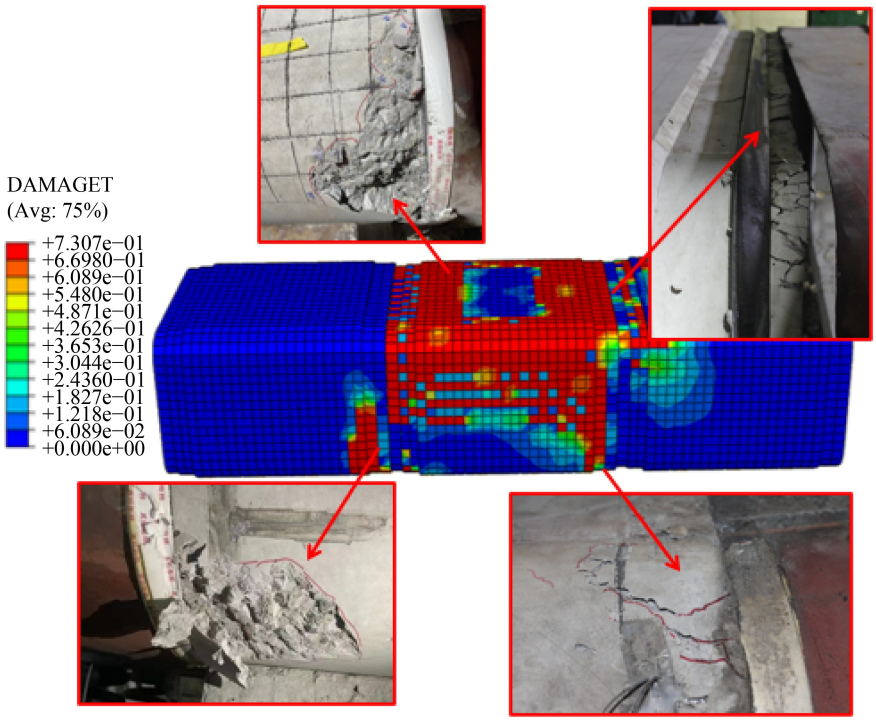

Fig. 14 Schematic of concrete damage.

3.2.2 Failure analysis of steel ring and pipe jack concrete of bending test

From Fig. 15, it can be noticed that in the numerical simulation of the bending test, a big opening took place at the bottom of the pipe segment, which is the final phase of the development of bending failure and is essentially in line with the failure process of the laboratory joint test. The bottom opening is regarded as a joint failure, and at this point, the steel sleeve ring is still within the elastic deformation range. Under bending failure circumstances, the overall damage of the pipe segment is smaller compared to that under shear failure conditions. The stress concentration of the steel sleeve ring is at the four chamfer locations, and it can also be witnessed that the steel sleeve ring bottom surface displays a certain degree of stress concentration owing to the pull of the chamfer. The main failure location of the concrete in the pipe segment joint is also focused on the four chamfer positions, with the top two chamfers being more prominent. Sidewall cracks also emerge in the chamfer of the joint, and the top surface of the concrete is the main load-bearing area, while the stress on the other parts of the concrete is relatively small. Once the joint is opened under bending failure, it is considered as joint failure, and therefore the damage range and severity are smaller than those under shear deformation conditions.

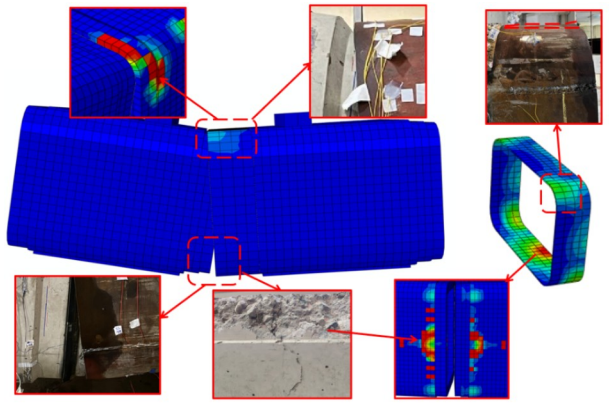

Fig. 15 Simulation results of bending failure.

3.2.3 Experimental and simulated load-displacement curves

Focusing on the deformation characteristics of shear failure, the shear force acting on the steel casing ring at the pipe joint along with the resulting shear displacement is chosen to shape a shear force-shear displacement curve, which is then compared with the curve derived from the test to confirm the accuracy of the numerical simulation results. The shear force and shear displacement of the steel casing ring are extracted and plotted as a shear force-shear displacement curve, which is then contrasted with the graph obtained from the test. The results are presented in Fig. 16.

Figure 16 presents the comparison curves of numerical simulation shear and experimental shear under diverse conditions. In the initial horizontal phase, no shear is generated, and the gap between the steel ring and the concrete narrows. In the second stage, the steel ring is in

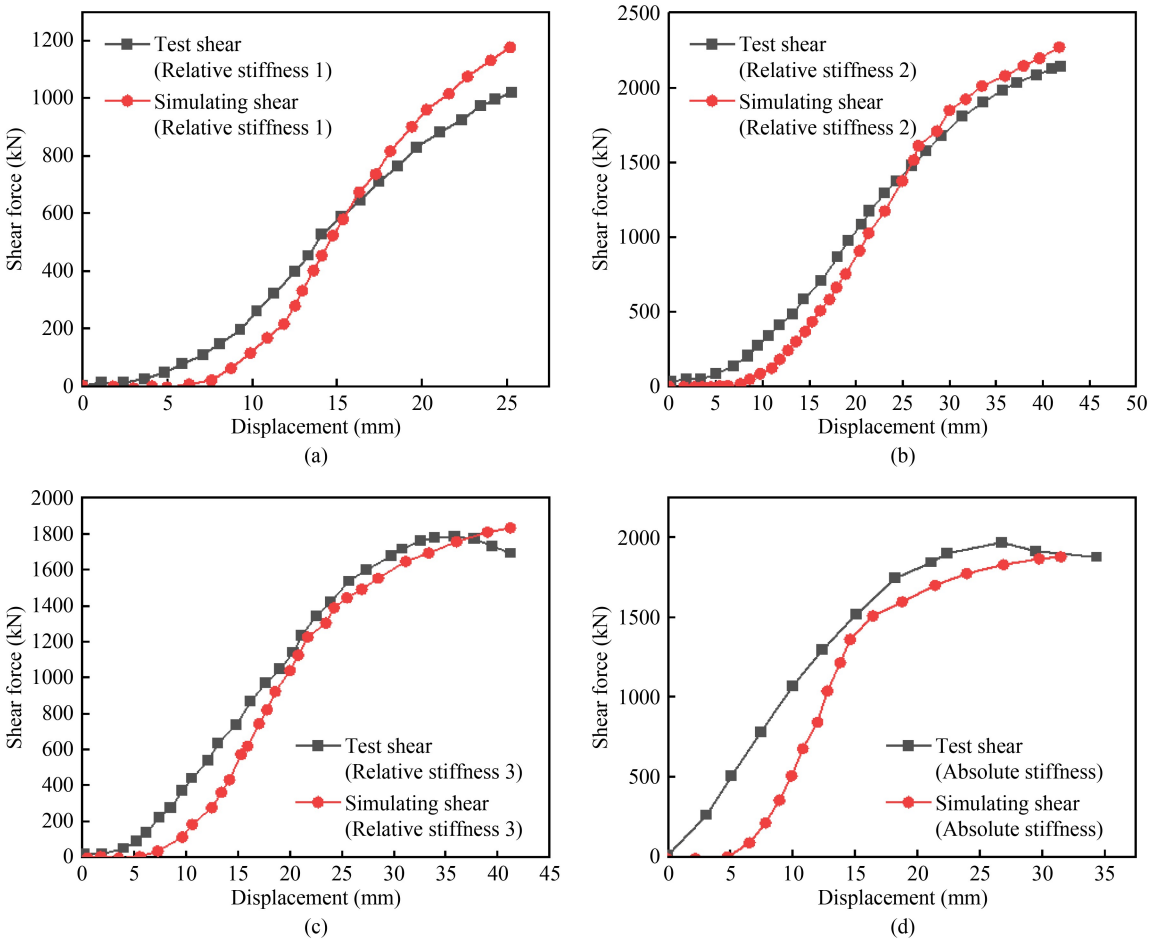

Fig. 16 Simulation comparison of shear failure test: (a) 9 springs; (b) 6 springs; (c) 4 springs; (d) 0 springs.

the elastic deformation phase, exhibiting a straight line ascending curve. In the third stage, the steel ring enters the yield stage, and it can be noticed that the growth rate of the curve lessens, and the shear resistance capacity of the steel ring is decreased. The progression trend of the numerical simulation results is in line with the experimental results.

The moment-rotation displacement curves obtained from the numerical simulation results are compared with the moment-rotation displacement curves obtained from the tests, and the results are shown in Fig. 17:

From Fig. 17, it can be observed that there exists a straight line segment in the numerical simulation curves under different circumstances. Because the three-dimensional refined numerical simulation nonlinear calculations, it is rather prone for the calculation to become non-convergent. Compared with the forces at the structural joint, the forces on the rubber ring can be roughly neglected. Consequently, the rubber ring at the joint was not taken into consideration, resulting in a certain gap at the joint. From the analysis of the numerical simulation results curve, it can be perceived that the numerical simulation results roughly align with the experimental conditions. As the strength of the foundation escalates, the bending resistance of the joint also gradually increases. The bending deformation of the joint primarily occurs in two phases: in the first phase, there is a gap between the steel casing ring and the concrete, and the opening angle increases without generating a moment; in the second phase, after the steel casing ring and the concrete come into contact, the moment gradually increases with the load, and the opening angle also gradually increases. During this stage, the steel casing ring remains within the elastic deformation range until the bottom of the joint is separated. Due to the assembly error in the laboratory test, there might be a gap between the steel casing ring and the joint concrete, which can give rise to the moment occurring at the initial stage of loading, resulting in a discrepancy in the initial rotation angle between the test and the simulation.

3.3 Numerical simulations of joint considering deformation discontinuity

Owing to the limitations of the experiment, it's not feasible to conduct tests on multiple pipe joints. Since there are relatively few pipe joints, the constraining effect

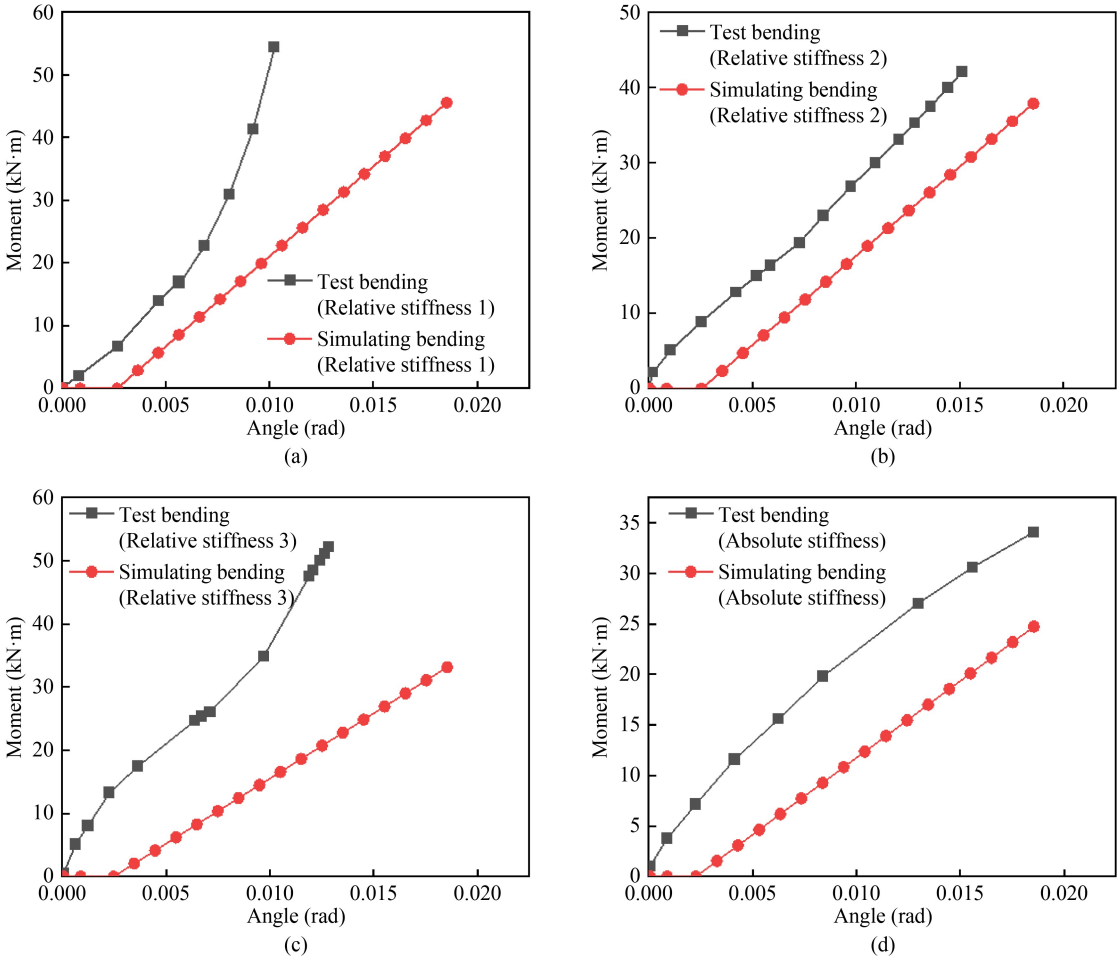

Fig. 17 Simulation comparison of bending failure test: (a) 9 springs; (b) 6 springs; (c) 4 springs; (d) 0 springs.

of the end joints on the middle joints is more prominent. Besides, there is rotational nonlinearity and the discontinuity of deformation between the pipe joints. Thus, following the same method as in building the above model, a three-dimensional refined model of five pipe joints is constructed. A vertical displacement is applied to the third pipe joint, and different foundation strengths are accomplished by setting diverse spring stiffnesses at the bottom of the pipe joints. This enables the exploration of the failure characteristics of the pipe joint under more realistic circumstances.

3.3.1 Model and parameter configuration

The model assembly is presented in Fig. 18: for the convenience of subsequent analysis, the pipe joints are labeled from left to right as 1, 2, 3, 4, and 5. The loading in this experiment employs displacement loading applied at the top of the 3rd pipe joint. Four displacement cases of 20, 30, 40, and 50 mm are selected for analysis. The horizontal movement in the plane direction of the pipe joints is not taken into account, and this direction is constrained. The interaction between the soil and the pipe joints is also simulated using foundation spring elements with the same spring stiffness as previously utilized. To avoid stress concentration, a steel plate is placed at the bottom of the pipe joint, with the steel plate and the pipe joint bottom having a binding effect. The springs are positioned on the bottom steel plate. To simulate the actual state and make the simulation more intuitive, the bottom of the 3rd pipe joint is equipped with 4 springs, the bottoms of the 2nd and 4th pipe joints are equipped with 6 springs, and the bottoms of the 1st and 5th pipe joints are fitted with 9 springs, as depicted in Fig. 18.

3.3.2 Deformation mechanism analysis of joint

After the calculation, the phenomena of the four cases are generally in accord, and the 50 mm displacement case is chosen for analysis. Figure 19 is a schematic diagram of the model calculation results.

From Fig. 19, it can be noted that under the displacement action at the top of the 3rd pipe joint, the overall deformation is roughly symmetric from left to right, and the stress is approximately centrosymmetric distributed. Due to the variations in the spring stiffness at the bottom and the structure of the socket, there are certain discrepancies in the displacement of each pipe

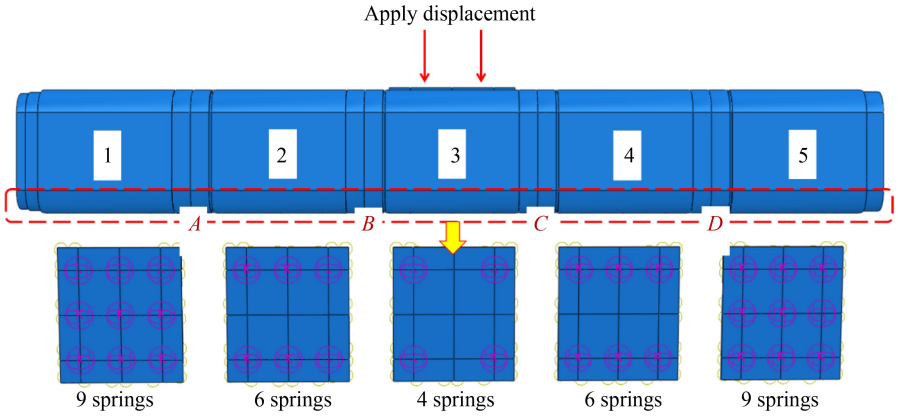

Fig. 18 Overview of the model.

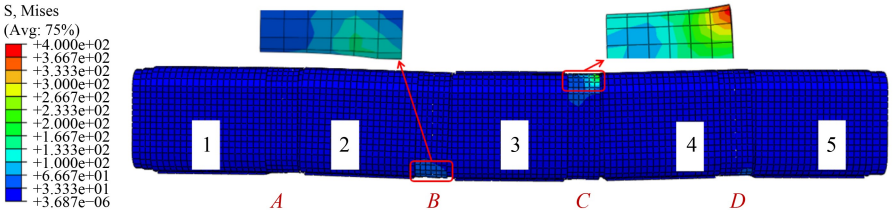

Fig. 19 Calculation results.

joint and the stress of the steel casing ring. Simultaneously, it can be identified that since the model utilizes multiple pipe joints and the ends are not constrained, the influence of the boundary conditions at the ends is eliminated, thus the relative displacement between the pipe joints and the joint deformation is relatively more in line with the actual scenario. The simulated results of the failure phenomenon are consistent with those in the preceding text, but the overall deformation and destruction degree are smaller than those in the previous experimental and simulation studies, further reflecting the more realistic characteristics of joint failure and deformation.

The concrete damage of the pipe joints is shown in Fig. 20. The damage to the concrete of the pipe joint lies at the chamfer of the joint, where the stress is significantly greater than that of other parts of the joint due to stress concentration. Via the previous laboratory joint test and this numerical simulation, it can be observed that the deformation and failure law of the pipe joint is as follows: at the initial loading phase, the steel casing ring has not yet come into contact with the pipe joint concrete due to a certain gap; as the loading proceeds, the steel casing ring contacts the joint concrete, and at this point, it is in a relatively good linear elastic deformation stage, with stress and deformation primarily located at the chamfer positions of the load-bearing side of the concrete and the steel casing ring, and the stress generated by the side wall of the pipe joint is not significant; as the loading continues, the steel casing ring gradually warps and bulges, and the joint concrete undergoes damage, with the stress on the load-bearing

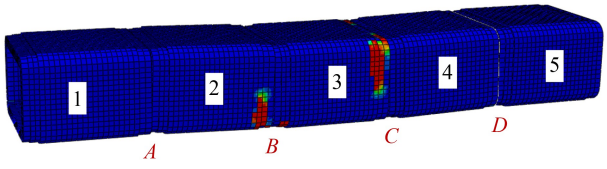

Fig. 20 Concrete damage diagram.

side further increasing; in the final stage, if the loading continues, the joint will experience separation at the bottom and failure of the steel casing ring.

To further probe into the deformation mechanisms of the joints under diverse foundation strengths, the four joints among the five pipe joints are labeled from left to right as A to D. The misalignment is computed as the distinction between the next pipe joint and the preceding one (with the sign), and the opening is positive at the bottom while negative at the top. The misalignment and opening of each joint under the four operating conditions are singled out separately and plotted into the joint deformation curves presented in Fig. 21.

From Fig. 21, it can be noticed that as the vertical displacement applied to the top of the 3rd pipe joint goes up, the maximum values of the misalignment and opening also rise accordingly. The slope of the curves between adjacent joints gradually escalates, suggesting that the distinction in misalignment and opening becomes more prominent. In the analysis, the progressively increasing vertical displacements from 20 to 50 mm are interpreted as a gradual decline in the foundation strength and an enlarging difference in foundation strength between adjacent pipe joints. As this grows, the misalignment and

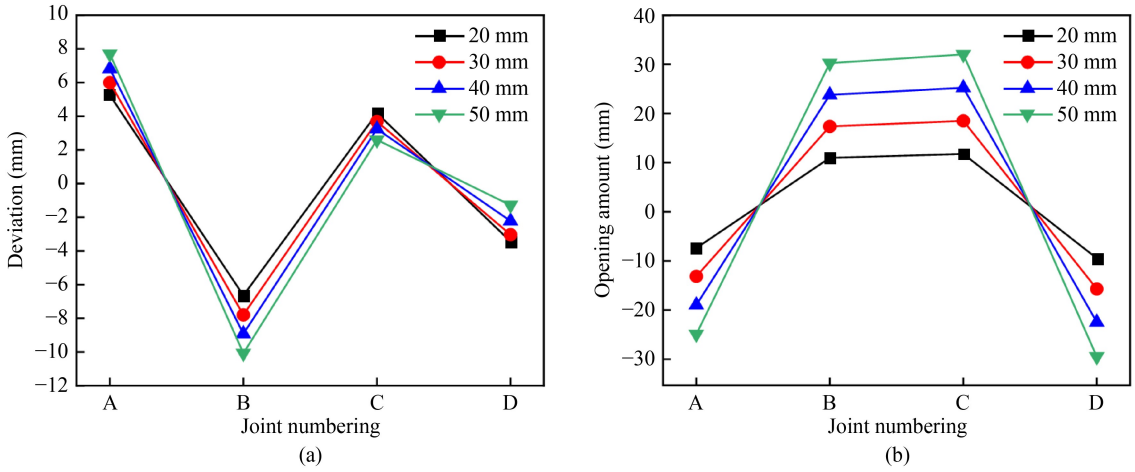

Fig. 21 Joint deformation curves: (a) misalignment; (b) horizontal opening.

the variation in misalignment between adjacent joints also rise, resulting in an increase in the opening and the variation in opening between adjacent joints. This could potentially give rise to the failure of the joints within the range, causing water leakage and affecting the normal usage of the tunnel.

The design parameters of the steel casing ring will affect its performance. The main design parameters of the steel casing ring are its thickness and width. Based on this, while keeping the 50 mm vertical displacement unchanged, several different operating conditions were chosen for numerical simulation, including the thickness of the steel casing ring at 12, 15 (the original model size), and 18 mm, and the width of the steel casing ring at 310, 320 (the original model size), and 330 mm. This was done to look into the influence of the design parameters of the steel casing ring on the joint deformation. The simulation data results are presented in Fig. 22.

An increment in the thickness of the steel casing ring shows an increment in its stiffness, which in turn boosts its capacity to resist deformation. As the thickness of the steel casing ring goes up, the opening and misalignment at the joint will correspondingly go down. On the flip side, an increase in the width of the steel casing ring will raise its effective area, thereby strengthening its resistance to deformation. With the rise in the width of the steel casing ring, the misalignment and opening between the pipe joints will also fall.

4 The shell-joint theoretical model for rectangular pipe-jacking tunnels

The results of the laboratory joint test and the refined numerical simulation show that the joint failure mainly takes place in three phases: closure of the gap, force, and deformation failure of the steel sleeve ring. The ultimate failure in both instances occurs at the chamfer of the steel sleeve ring, indicating that the shear and bending resistance of the joint are shouldered by the steel sleeve ring. This implies that the joint of the rectangular pipe-jacking tunnel presents significant discontinuity and nonlinearity.

By combining similar rectangular pipe-jacking tunnel

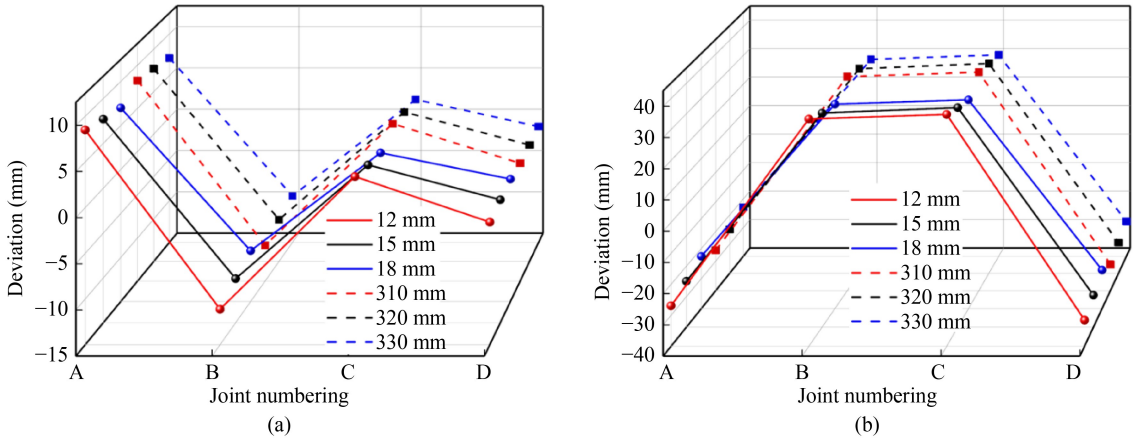

Fig. 22 Calculation results for different thicknesses and widths of steel casing rings: (a) misalignment with different thicknesses and widths of steel casing rings; (b) horizontal opening with different thicknesses and widths of steel casing rings.

projects, it can be seen that joint failure mainly occurs in the phases of gap closure, force on the steel sleeve ring, and deformation failure. The ultimate failure in both tests takes place at the chamfer of the steel sleeve ring, indicating that the shear and bending resistance of the joint are shouldered by the steel sleeve ring. This also shows that the joint of the rectangular pipe-jacking tunnel has significant discontinuity and nonlinearity.

The joint mainly withstands bending moments around the radial direction of the tunnel, shear forces along the tangential direction of the tunnel, and axial forces along the axial direction of the tunnel, as depicted in Fig. 23. (*Y*: tangential direction of the tunnel; *X*: radial direction of the tunnel; *Z*: axial direction of the tunnel; *M*: bending moment of the joint around the tunnel *X*; *F*: axial force along the tunnel *Z*; *Q*: shear force along the vertical *Y* of the tunnel.)

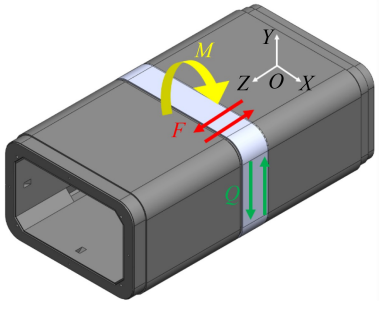

Fig. 23 Rectangular pipe-jacking tunnel force diagram.

4.1 Model structure

The refined finite-element model can accurately reproduce the behavior of joints, yet it has drawbacks such as high consumption of computing resources, heavy computational load, and poor convergence. To address these issues, this study proposes a shell-joint theoretical model for rectangular pipe-jacking tunnels. The joint connectors established through this model can effectively reduce the computation time of FEM software, ensure decent accuracy, and also offer certain guidance for the mechanical behavior of rectangular pipe-jacking tunnels. Combining the analysis of the mechanical properties of the joint in the rectangular pipe-jacking tunnel from the previous sections, a shell-joint theoretical model for the rectangular pipe-jacking tunnel is set up. The shell-joint theoretical model for rectangular pipe-jacking tunnels is a simplified theoretical model, which is applicable to the overall structural analysis and parameter optimization of long-distance rectangular pipe-jacking tunnels. This model simplifies the rectangular pipe-jacking segments to shell structures and employs a novel combination of mechanical elements to simulate the mechanical properties of the joints between the segments. The combination of mechanical elements encompasses rotational dynamic elements and shear dynamic elements, as shown in Fig. 24. In the figure: red round shape stands for rotational dynamic elements; red squares shape stand for shear dynamic elements.

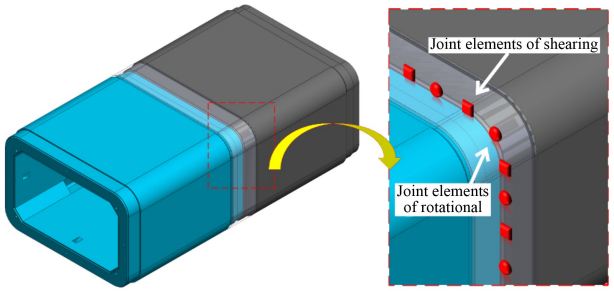

Fig. 24 Shell-Joint theoretical model.

By dissecting the rotational dynamic elements and shear dynamic elements in the shell-joint theoretical model of the rectangular pipe-jacking tunnel, five fundamental mechanical elements can be acquired, which are the friction limit stop, the friction plate, the compression limit stop, the torsion spring, and the tension-compression spring. By combining these five fundamental mechanical elements, the mechanical properties of the joint in the rectangular pipe-jacking tunnel can be emulated. The five fundamental mechanical elements are displayed in Fig. 25. In the figure: *i* and *j* are the calculation points necessary for the analysis of the basic mechanical elements.

The corresponding mechanical properties of the joints for each basic mechanical element are presented in Table 3.

Combining the basic mechanical elements, two types of joint mechanical elements for simulating tunnel joints are obtained as shown in Fig. 26.

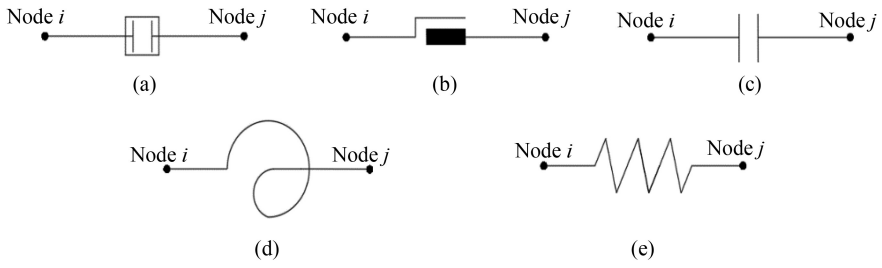

Fig. 25 Five basic mechanical elements.

Table 3 Mechanical properties of joints corresponding to the five basic elements

Name	Mechanical properties simulated.
Frictional restriction	The pipe-jacking joints have a certain amount of shear displacement.
Frictional plate	The concrete contact surface of the pipe-jacking joints has a frictional effect.
Compression restriction	The concrete of the pipe-jacking joints is essentially incompressible.
Rotational spring	The pipe-jacking joints rotate around the tunnel's radial direction.
Dual-action spring	The steel ring undergoes tensile and compressive forces.

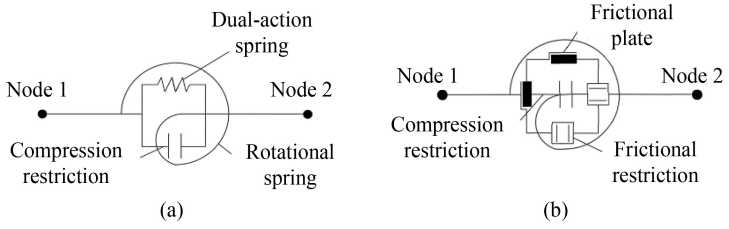

Fig. 26 Two types of joint mechanical elements: (a) rotational dynamic elements; (b) shear dynamic elements.

The rotational dynamic element comprises the compression limit stop, the torsion spring, and the tension-compression spring elements. The compression limit stop and the tension-compression spring form a one-directional tensile spring, which can imitate the opening and compression of the pipe segment joint under tension. However, because of the relatively big concrete stiffness, there essentially exists no compressive deformation; the torsion spring can simulate the rotation of the pipe segment joint under the action of the bending moment. The shear dynamic element is composed of the friction limit stop, the compression limit stop, and the bidirectional friction plate elements. The friction limit stop can control the maximum shear displacement generated by the pipe segment joint under the action of the tangential shear force, the compression limit stop can confine the longitudinal compression deformation of the pipe segment, and the bidirectional friction plate can imitate the shear displacement generated by the pipe segment joint under the action of the tangential shear force.

4.2 Joint connector element

To define the stiffness matrix of the joint element for the rectangular pipe-jacking tunnel, a local coordinate system is first defined for the joint element, as shown in Fig. 27.

In the local coordinate system, t stands for the tangential direction of the pipe segment, n represents the radial direction of the tunnel, and s denotes the longitudinal direction of the tunnel. The discontinuity at the joint between adjacent pipe segments is indicated by the relative displacement of any two nodes m and n at the joint in the local coordinate system n, s. Both m and n are the calculation points needed for the analysis of the joint connection element.

Each joint connection element comprises two nodes (node m and node n), and the displacement vector $\boldsymbol{D}$ of each node in the local coordinate system of the joint connection element can be represented as:

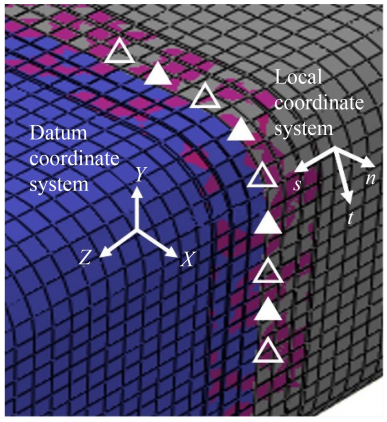

Fig. 27 Local coordinate system of the joint connection element.

$$\boldsymbol{D} = (n_m t_m s_m \theta_{nm} \theta_{tm} \theta_{sm})^{\mathrm{T}}, \qquad r = m, n. \tag{23}$$

The relative displacement between the nodes, $\Delta\boldsymbol{d}$, can be expressed as:

$$\begin{aligned}\Delta\boldsymbol{d} &= (\Delta n\ \Delta t\ \Delta s\ \Delta\theta_n\ \Delta\theta_t\ \Delta\theta_s)^{\mathrm{T}} \\ &= (n_m - n_n\ t_m - t_n\ s_m - s_n\ \theta_{nm} - \theta_{nn}\ \theta_{tm} - \theta_{tn}\ \theta_{sm} - \theta_{sn})^{\mathrm{T}}.\end{aligned} \tag{24}$$

In the equation, n_m, t_m, and s_m represent the displacement components of the lower-indexed node along the n, t, and s axes, respectively; n_n, t_n, and s_n represent the displacement components of the upper-indexed node along the n, t, and s axes, respectively; θ_{nm}, θ_{tm}, and θ_{sm} represent the rotational components of the m node along the n, t, and s axes, respectively; θ_{nn}, θ_{tn}, and θ_{sn} represent the rotational components of the n node along the n, t, and s axes, respectively.

Similarly, the external forces F carried by the joint element can be expressed as:

$$\boldsymbol{F} = (F_n\ F_t\ F_s\ M_n\ M_t\ M_s)^{\mathrm{T}}. \tag{25}$$

According to the characteristics of the rectangular pipe-jacking tunnel structure, the unit stiffness matrix $\boldsymbol{K}^{\mathrm{R}}$ of the rotational dynamic element at the pipe segment joint is represented as:

$$\boldsymbol{K}^{\mathrm{R}} = \begin{pmatrix} 0 & 0 & 0 & 0 & 0 & 0 \\ 0 & 0 & 0 & 0 & 0 & 0 \\ 0 & 0 & K_s^{\mathrm{R}} & 0 & 0 & 0 \\ 0 & 0 & 0 & 0 & 0 & 0 \\ 0 & 0 & 0 & 0 & 0 & 0 \\ 0 & 0 & 0 & 0 & 0 & K_{\theta n}^{\mathrm{R}} \end{pmatrix}. \tag{26}$$

In the equation, $K_{\mathrm{s}}^{\mathrm{R}}$ stands for the stiffness of the one-directional tension spring. The stiffness of the one-directional tension spring refers to the tensile force applied by the steel sleeve ring on the joint, which is the ratio of the friction force F_{r} between the steel sleeve ring and the concrete pipe segment to the deformation Δu of the steel sleeve ring under the applied force. Thus, the stiffness of the one-directional tension spring can be calculated via Eq. (21):

$$K_{\mathrm{s}}^{\mathrm{R}} = \frac{F_{\mathrm{r}}}{\Delta u}. \tag{27}$$

In the equation, F_{r} stands for the frictional resistance between the steel sleeve ring and the concrete of the pipe segment spigot; Δu indicates the elongation of the steel sleeve ring when it gets stretched. When the pipe segments of a rectangular pipe-jacking tunnel are assembled, the spigot concrete and the sealing rubber gasket form a socket-and-spigot relationship under the effect of the assembly force, and the steel sleeve ring at the pipe segment socket compresses the rubber gasket. At this moment, the result of the contact stress on the rubber gasket and the contact area is the normal force at the contact interface at that position. According to the principles of tribology, the frictional resistance F_{r} between the steel sleeve ring and the concrete of the pipe segment spigot can be attained by multiplying the normal force at the contact interface by the coefficient of dynamic friction μ_{r} of the rubber gasket. In short, the frictional resistance F_{r} is calculated by multiplying the normal force (contact stress times contact area) with the coefficient of dynamic friction μ_{r} of the rubber gasket.

$$F_{\mathrm{r}} = \mu_{\mathrm{r}}\left[0.51\left(\frac{h_1}{2}\right)(4a+4b+2\pi r)\right]. \tag{28}$$

In the equation, F_{r} denotes the frictional force between the annular steel sleeve ring and the concrete pipe segment; h_1 is the length of the water-facing surface of the sealing rubber gasket; μ_{r} is the coefficient of dynamic friction between the sealing rubber gasket and the concrete, having a value of 0.45 based on the experimental results.

The stiffness $K_{\theta n}^{\mathrm{R}}$ of the pipe segment joint signifies the deformation of the joint under the bending moment M, which is the equivalent bending stiffness of the joint.

$$K_{\theta n}^{\mathrm{R}} = \frac{M}{\Delta\theta}. \tag{29}$$

To determine the equivalent bending stiffness of the rectangular pipe-jacking joint, the following basic assumptions are made: The bending deformation of the rectangular pipe-jacking joint is assumed to follow the plane section assumption, meaning that the shear deformation is much smaller than the bending deformation, and the plane section assumption is approximately applicable. The pipe segment is regarded as having its axis of symmetry as the balancing line. In the tension zone of the pipe segment, the steel sleeve ring undergoes uniform tensile stress, while in the compression zone, only the concrete of the pipe segment experiences compressive stress, and it is assumed to be in an ideal elastic state. The equivalent elastic modulus of E_{s} of the steel ring when uniformly distributed along the cross-section is defined. The calculation method is as shown in Eq. (24).

$$E_{\mathrm{s}} = \frac{E_{\mathrm{r}}A_{\mathrm{s}}}{A_{\mathrm{c}}}. \tag{30}$$

In Eq. (24), E_{s} stands for the elastic modulus of the steel sleeve ring; A_{s} is the cross-sectional area of the steel sleeve ring along the circumference of the tunnel; and A_{c} is the cross-sectional area of the concrete pipe segment of the rectangular pipe-jacking tunnel.

Based on the dynamic equilibrium conditions and deformation compatibility conditions of elastic bodies, the distance of l between the medians of adjacent pipe segments is regarded as the calculation unit. When a pipe segment undergoes a bending moment of M, it experiences bending deformation, and the medians of the adjacent pipe segments extend and intersect, forming a rotation angle of θ. The bending deformation of the pipe segment is depicted in Fig. 28.

Under elastic conditions, the longitudinal cross-sectional dimensions and deformation stress diagram of the rectangular pipe-jacking joint are presented in Fig. 29(a). In the figure, m and n are the distances from the centerline of the tunnel section to the x-axis and y-

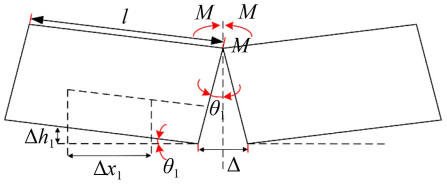

Fig. 28 Diagram of bending deformation of the pipe element.

axis, respectively; t_1 and t_2 are the thicknesses of the short and long sides of the pipe segment (both being uniformly taken as t); and h is the distance of the neutral axis from the long axis of the rectangular section. A calculation model as shown in Fig. 29(b) is selected for analysis, and its deformation compatibility equation is:

$$\begin{cases}\delta_{s(max)} = (n+h)\theta, \\ \delta_{c(max)} = (n-h)\theta, \end{cases} \tag{31}$$

where E_s is the equivalent elastic modulus distributed along the cross-section of the steel casing ring; E_c is the elastic modulus of the pipe joint concrete; A_c is the cross-sectional area of the concrete pipe joint in a rectangular pipe-jacking tunnel; calculated by taking the length l between the centerlines of adjacent pipe joints as a unit; l_s is the length along the longitudinal direction of the tunnel that the steel casing ring is distributed over. $\varepsilon_{s(max)}$ and $\varepsilon_{c(max)}$ are the maximum tensile and compressive strains of the pipe joint section. From the force balance condition of the pipe joint, it can be derived that:

$$\begin{aligned}&\frac{E_s}{l_s}\int_{-n}^{h}(h-y)t\mathrm{d}y + \frac{n+h}{l_s}E_s mt \\ =&\frac{E_c}{l}\int_{h}^{n}(y-h)t\mathrm{d}y + \frac{n-h}{l}E_c mt.\end{aligned} \tag{32}$$

Similarly, from the moment balance condition, it can be derived that:

$$\begin{aligned}&2\frac{E_s}{l_s}\theta\int_{-n}^{h}(h-y)^2 t\mathrm{d}y + 2\theta\frac{n+h}{l_s}E_s mt(n-h) \\ &+2\frac{E_c}{l}\theta\int_{h}^{n}(y-h)^2 t\mathrm{d}y + 2\theta\frac{(n^2-h^2)}{l}E_c mt = M.\end{aligned} \tag{33}$$

By combining Eqs. (25) to (27), it can be concluded that:

$$\begin{aligned}\theta = &\frac{M}{2E_s\frac{t}{l_s}\left[\frac{1}{3}(h^3+n^3)-h(h^2-n^2)+h^2(h+n)\right]+2\frac{n+h}{l_s}E_s mt(n-h)} \\ &+2\frac{n^2-h^2}{l}E_c mt + 2E_c\frac{t}{l}\left[\frac{1}{3}(n^3-h^3)-h(n^2-h^2)+h^2(n-h)\right].\end{aligned} \tag{34}$$

From the formula for the rotation of an equivalent continuous beam:

$$\theta = \frac{Ml}{(EI)_{eq}}. \tag{35}$$

In the formula, $(EI)_{eq}$ stands for the longitudinal equivalent bending stiffness. By combining Eqs. (28) and (29), the longitudinal equivalent bending stiffness of the rectangular pipe-jacking tunnel can be obtained as follows:

$$\begin{aligned}(EI)_{eq} = &2E_s\frac{tl}{l_s}\left[\frac{1}{3}(h^3+n^3)-h(h^2-n^2)+h^2(h+n)\right] \\ &+2l\frac{n+h}{l_s}E_s mt(n-h)+2(n^2-h^2)E_c mt \\ &+2E_c t[1/3(n^3-h^3)-h(n^2-h^2)+h^2(n-h)].\end{aligned} \tag{36}$$

The element stiffness matrix $\boldsymbol{K}^S$ for the shear mechanical components at the pipe joint connection is expressed as:

$$\boldsymbol{K}^S = \begin{pmatrix} K_n^S & 0 & 0 & 0 & 0 & 0 \\ 0 & K_t^S & 0 & 0 & 0 & 0 \\ 0 & 0 & K_s^S & 0 & 0 & 0 \\ 0 & 0 & 0 & 0 & 0 & 0 \\ 0 & 0 & 0 & 0 & 0 & 0 \\ 0 & 0 & 0 & 0 & 0 & K_{\theta n}^R \end{pmatrix}, \tag{37}$$

where $K_{\theta n}^R$ is the stiffness of the pipe joint connection, as mentioned earlier; K_s^R is the stiffness of the compression limiting element, and it can be expressed as:

$$K_s^R = \begin{cases} 0, & \Delta s \geqslant 0, \\ \infty, & \Delta s < 0 \end{cases}. \tag{38}$$

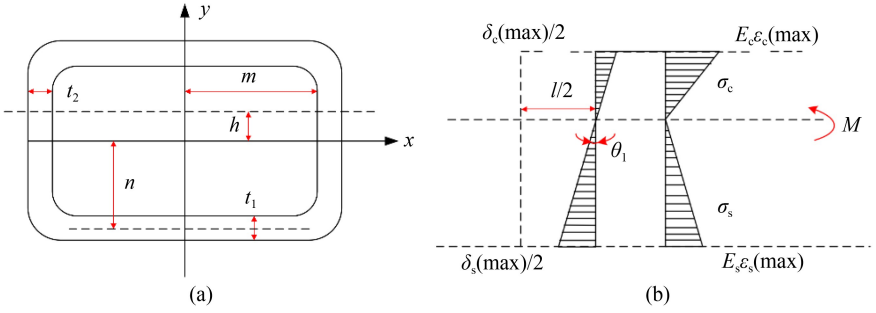

Fig. 29 Simplified mechanical model diagram: (a) cross-sectional dimensions; (b) stress diagram.

K_n^S and K_t^S are both the shear stiffness at the pipe joint connection, which can be expressed as:

$$K_{n(t)}^S = \begin{cases} \infty, & |F_{n(t)}| \leqslant Q, \\ \dfrac{|F_{n(t)}|}{\delta_{n(t)}}, & |F_{n(t)}| > Q,\ \Delta n(t) < \delta_{n(t)}. \end{cases} \tag{39}$$

In the formula, $\delta_{n(t)}$ denotes the maximum permitted shear displacement at the pipe joint along the n-axis and t-axis, while $Q_{n(t)}$ signifies the ultimate sliding frictional resistance at the joint along the n-axis and t-axis. Via modifying Eq. (34), it can be derived as follows:

$$Q_{n(t)} = \mu_{n(t)} F_f. \tag{40}$$

In the formula, $\mu_{n(t)}$ stands for the friction coefficient on the contact surface along the n-axis and t-axis at the pipe joint; F_f refers to the frictional resistance about the contact area between the pipe and soil, as well as between the pipe and slurry, taking into account the unit length of the pipe joint. It can be roughly calculated using Eq. (35) as follows:

In line with the principles of tribology, the frictional resistance F_f of a rectangular pipe-jacking tunnel in contact with soil/slurry can be acquired by transforming the normal force at the contact interface. This is reckoned as the soil pressure acting on the jacking pipe structure multiplied by the dynamic friction factor μ_f for the pipe-soil/slurry contact situation. The soil pressure can be computed by the full soil column theory, as depicted in Fig. 30. Throughout the calculation, half of the structure is chosen to erect a force analysis diagram for analysis.

$$\begin{cases} q_1 = \gamma H, \\ q_2 = \gamma (H + r - r\sin\theta), \\ q_3 = W/[2(a+r)], \\ e_1 = K_0 q_2, \\ e_1 = K_0 \gamma (H + r + 2b + r\sin\theta). \end{cases} \tag{41}$$

In the formula: γ denotes the natural unit weight of the soil; H represents the buried depth of the pipe-jacking tunnel; a and b are the half-width and half-height of the pipe-jacking tunnel, excluding the length of the chamfered circular arc; r is the radius of the chamfer at the four corners of the rectangular pipe-jacking tunnel; W is the self-weight of the jacking structure; q_1 and q_2 are the vertical stratum pressures acting on the top and bottom surfaces of the pipe-jacking tunnel, respectively; q_3 is the structural self-weight acting on the bottom surface of the pipe-jacking; e_1 and e_2 are the horizontal stratum pressures acting on the top and bottom surfaces of the side walls of the pipe-jacking tunnel, respectively; K_0 is the coefficient of passive earth pressure. Thus, the frictional resistance F_f per unit length of the pipe joint is:

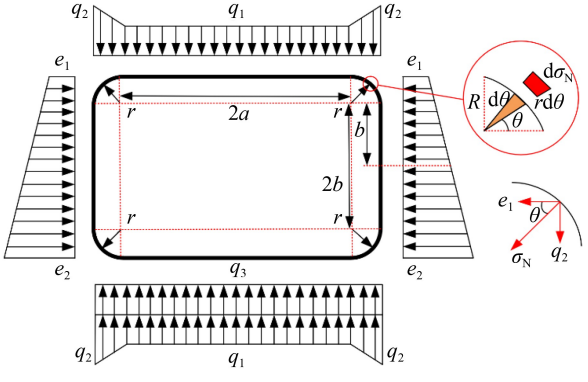

Fig. 30 Calculation diagrams of normal force of rectangular pipe-jacking contact surface.

$$\begin{aligned} F_f = \mu_f \Big[& 2\Big(\Big(\int_0^{\pi/2} q_2 \sin\theta + e_1 \cos\theta\Big) r\mathrm{d}\theta \\ & + \Big(\int_0^{\pi/2} (q_2 + q_3)\sin\theta + e_2 \cos\theta\Big) r\mathrm{d}\theta \\ & + 2K_0 (q_1 + \gamma(r+b))b\Big) + 4q_1 a + W\Big]. \end{aligned} \tag{42}$$

$$\mu_f = \mu_s \frac{\varepsilon}{2\pi} + \mu_m \left[1 - \frac{\varepsilon}{2\pi(1+e)}\right]. \tag{43}$$

In the formula: F_f is the resultant frictional force per unit length on the pipe joint; ε is the contact angle between the pipe joint and the soil; μ_f is the effective friction coefficient, which is determined using geometric relationships and whose value is related to the contact angle ε; μ_s and μ_m are the dynamic friction coefficients for the pipe-soil and pipe-slurry contact interfaces, respectively, with values of 0.3 and 0.01; e is the soil porosity. When the concrete at the pipe joint connection is mutually compressed, F_f assumes a positive value; when the spigot of the pipe joint detaches from the steel casing ring, F_f assumes a negative value.

Consequently, by calculating the stiffness in each direction of each joint connection element to form its stiffness matrix, the relationship between the nodal forces and deformations of the joint element can be expressed as:

$$\boldsymbol{F} = \boldsymbol{K}(\Delta \boldsymbol{d}). \tag{44}$$

In the formula: $\boldsymbol{K}$ represents the stiffness matrix of the joint element in local coordinates.

To transform the stiffness matrix $\boldsymbol{K}$ to the global coordinate system, the transformed stiffness matrix $\boldsymbol{K}$' can be represented as:

$$\boldsymbol{K}' = \boldsymbol{L}^T \boldsymbol{K} \boldsymbol{L}. \tag{45}$$

$$\boldsymbol{L} = \begin{pmatrix} \boldsymbol{\lambda} & 0 \\ 0 & \boldsymbol{\lambda} \end{pmatrix}. \tag{46}$$

$$\boldsymbol{\lambda}=\begin{pmatrix}\lambda_{nx} & \lambda_{ny} & \lambda_{nz}\\ \lambda_{tx} & \lambda_{ty} & \lambda_{tz}\\ \lambda_{sx} & \lambda_{sy} & \lambda_{sz}\end{pmatrix}. \tag{47}$$

In the formula: L denotes the transformation matrix; λ_{nx} stands for the cosine of the angle between the n-axis and the x-axis, and likewise for the other angles.

4.3 Finite element simulation of shell-joint behavior

4.3.1 Creation of numerical model

A shell-joint numerical calculation model is constructed based on the dimensions of the test specimen and the load boundary conditions in the joint test. The pipe joint is modeled by using three-dimensional shell elements with a cross-sectional size of 1625 mm × 1075 mm, and a longitudinal width of 1500 mm. The concrete strength grade utilized is C50, having an elastic modulus of 3.45×10^7 kPa. A bushing connector is employed to connect the pipe joints, with the stiffness values selected by the laboratory joint test loading section. Normal springs are established within the model to simulate ground constraints.

From the curve variation pattern in Fig. 31(a), it can be perceived that the calculation results of the shell-joint model are in good agreement with the test results, but there exists a certain disparity in the maximum shear displacement, mainly because in the joint shear test, the assembly error of the specimen gives rise to a certain amount of reverse displacement, thereby resulting in a greater shear amount obtained in the test compared to the actual allowable shear displacement. The moment-rotation angle curve alterations during the simulation process of the shell-joint model are extracted and compared with the deformation results of the laboratory joint test, as shown in Fig. 31(b). It can be observed that the moment-relative rotation angle curve of the joint calculated numerically based on the shell-joint theoretical model follows the same basic change pattern as the moment-relative rotation angle curve derived from the test results. The descending section of the moment-rotation angle curve appears in Fig. 31(b). This is because when the rotation angle exceeds 0.08 radians, the chamfer of the steel sleeve ring yields (with a stress reaching 235 MPa) and the concrete chamfer is crushed. This leads to a reduction in the effective bearing area of the joint. At this point, the steel sleeve ring loses its elastic support capacity, and the concrete can no longer effectively transmit pressure. This reflects the nonlinear failure behavior of the joint, confirming that the numerical simulation calculation using the shell-joint theoretical model can effectively simulate the bending characteristics of the pipe segment joints.

In summary, by establishing the stiffness matrix of the mechanical unit at the joints of rectangular pipe-jacking tunnels and its calculation method, the numerical results of the shell-joint bending model and shear model were calculated and compared with the corresponding laboratory joint test results. The calculated results are in good agreement with the test results, verifying the accuracy and practicality of the shell-joint theoretical model. The above results demonstrate that the shell-joint theoretical model is well-suited for rectangular pipe-jacking tunnels with F-type socket and jack joints. However, in this study, the model was only verified by comparison with the results of large-scale tests and numerical simulations, lacking verification through comparison with on-site monitoring data from actual projects. Therefore, the next step of this research will focus on verifying the shell-joint theoretical model by comparing it with on-site monitoring data from actual projects, continue to optimize the shell-joint theoretical model, and consider the impact of complex strata simultaneously to expand its scope of application.

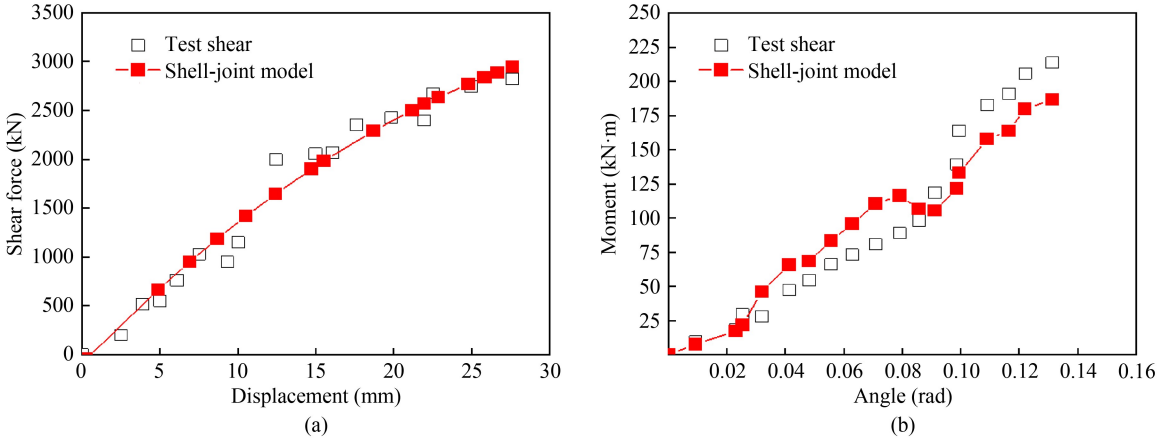

Fig. 31 Comparison of shell-joint numerical simulation results with experimental results: (a) comparison with shear test results; (b) comparison with bending test results.

5 Conclusions

1) Laboratory shear and bending tests have demonstrated that the failure process of joints in rectangular pipe-jacked tunnels is mainly divided into three phases: gap closure, steel ring force damage, and deformation damage. The ultimate failure usually takes place at the chamfer of the steel ring, suggesting that the shear and bending resistance of the joint is mostly borne by the steel ring. Specifically, in the case of shear failure, the central pipe section shows symmetric damage around the center and is prone to stress concentration at the chamfer; in the case of bending failure, the overall trend of the pipe section is characterized by top compression and bottom separation, with the steel ring undergoing buckling deformation as a result of the extrusion of the concrete.

2) A three-dimensional numerical model of the joint of a rectangular pipe-jacked tunnel was constructed using the ABAQUS finite element software. By varying different foundation stiffnesses, an in-depth investigation was carried out on the failure characteristics of the joint. In the shear model, the joint failure is evenly distributed around the central pipe section, with concrete damage, rebar yielding, and steel ring yielding all taking place at the chamfer. In the bending model, the joint failure is owing to the significant opening at the bottom of the pipe section, resulting in the joint separating. The force characteristics and failure modes of the joints in both the shear and bending models are in line with the experimental results, which confirms the accuracy and dependability of the numerical model.

3) Through establishing a three-dimensional refined numerical model for multiple joints of rectangular pipe-jacked tunnel sections, further exploration has been carried out into the deformation mechanisms and failure research of the joints under different foundation stiffnesses. It has been discovered that a reduction in foundation strength and an increase in the difference of foundation strength within the area can result in an increment in the misalignment, opening, differential misalignment, and differential opening of the pipe section joints. The analysis of the design parameters of the steel ring shows that increasing the width and thickness of the steel ring can enhance the stiffness of the joint and boost the joint's resistance to deformation.

4) A new model for rectangular pipe-jacking tunnels, namely the three-dimensional shell-joint model, is put forward, which simulates the pipe segments and the joints between them based on shell elements and joint units, and simulates the mechanical behavior of the actual rectangular pipe-jacking tunnel joints via the mechanical properties of the joint units. The stiffness matrix and its calculation method for the mechanical elements of rectangular pipe-jacking tunnel joints are also established. Meanwhile, by employing the shell-joint theoretical model to simulate the laboratory joint tests of rectangular pipe-jacking tunnels, it is discovered that the calculation results are in good agreement with the tests, confirming the accuracy and practicality of the shell-joint theoretical model.

Acknowledgements The authors gratefully acknowledge the financial support provided by the National Natural Science Foundation of China (Grant Nos. 51868062 and 52168060) and by the Innovation Scholarship for Doctoral Students of Beijing University of Technology.

Competing interests The authors declare that they have no competing interests.

References

1. Liu K, Xiao A, Zhang P, Zhou H, Chen Z, Xu T, Ma B, Ai H, Wang Q. Study on mechanical response of steel pipe-jacking considering the effect of pipe sticking. Tunnelling and Underground Space Technology, 2022, 127: 104617
2. Ma P, Shimada H, Huang S, Moses D N, Zhao G, Ma B. Transition of the pipe-jacking technology in Japan and investigation of its application status. Tunnelling and Underground Space Technology, 2023, 139: 105212
3. Ma P, Shimada H, Sasaoka T, Moses D N, Matsumoto F, Chen X. Investigation on the engineering effects of the geometrical configuration of the jacking rectangular pipe. Tunnelling and Underground Space Technology, 2022, 119: 104239
4. Xu X, Tong L, Li Z, Liu X, Hu Q, Yao H, Li J. Influence of extreme shallow jacked box tunnelling on underlying metro tunnels: A case study. Underground Space, 2023, 12: 234–250
5. Yang Y F, Liao S M, Liu M B, Wu D P, Pan W Q, Li H. A new construction method for metro stations in dense urban areas in Shanghai soft ground: Open-cut shafts combined with quasi-rectangular jacking boxes. Tunnelling and Underground Space Technology, 2022, 125: 104530
6. Ma P, Shimada H, Sasaoka T, Hamanaka A, Moses D N, Dintwe T K M, Matsumoto F, Ma B, Huang S. A new method for predicting the friction resistance in rectangular pipe-jacking. Tunnelling and Underground Space Technology, 2022, 123: 104338
7. Wang L, Chen X, Su D, Liu S, Liu X, Jiang S, Gao H, Yang W. Mechanical performance of a prefabricated subway station structure constructed by twin closely-spaced rectangular pipe-jacking boxes. Tunnelling and Underground Space Technology, 2023, 135: 105062
8. Wang L, Chen X, Su D, Zhou W, Sun B, Pan J, Wu Y, Feng M. Construction of a super-large prefabricated rectangular tunnel beneath a box culvert using pipe-jacking: A case study. Tunnelling and Underground Space Technology, 2024, 152: 105913
9. Li X J, Yan Z G, Wang Z, Zhu H H. Experimental and analytical study on longitudinal joint opening of concrete segmental lining. Tunnelling and Underground Space Technology, 2015, 46: 52–63
10. Liu X, Bai Y, Yuan Y, Mang H A. Experimental investigation of the ultimate bearing capacity of continuously jointed segmental tunnel linings. Structure and Infrastructure Engineering, 2016,

12(10): 1364–1379

11. Wang Z, Wang L Z, Li L L, Wang J C. Failure mechanism of tunnel lining joints and bolts with uneven longitudinal ground settlement. Tunnelling and Underground Space Technology, 2014, 40: 300–308
12. Zhang P, Ma B, Zeng C, Xie H, Li X, Wang D. Key techniques for the largest curved pipe-jacking roof to date: A case study of Gongbei tunnel. Tunnelling and Underground Space Technology, 2016, 59: 134–145
13. Kong C, Gao X, Wang F, Wang H, Li H, Zhao X, Liu J, Zhang Y, Luo Y. Analysis of mechanical properties and joint selection for secondary linings in drill and blast tunnels with prefabricated invert arch: Case study of a single-line railway tunnel. Tunnelling and Underground Space Technology, 2024, 144: 105560
14. Zhang J, Zhao M. Experimental study on the mechanical properties of longitudinal joints of shield tunnels under large deformation conditions. Tunnelling and Underground Space Technology, 2024, 144: 105447
15. Zhou L, Yan Z, Shen Y, Guan L. Experimental study on effect of ductile-iron panel stiffness on mechanical properties of segmental joints of shield tunnels. Underground Space, 2022, 7(6): 1056–1067
16. Zhu Y, Zhang Z, Huang X, Zhang G. Prototype loading tests on full-ring segmental lining of rectangular shield tunnel. Journal of Shanghai Jiaotong University (Science), 2018, 23(6): 746–757
17. Liu X, Zhang C, Zhang C, Yuan Y. Ultimate load-carrying capacity of the longitudinal joints in segmental tunnel linings. Structural Concrete, 2017, 18(5): 693–709
18. Liu X, Liu Z, Ye Y, Bai Y, Zhu Y. Mechanical behavior of quasi-rectangular segmental tunnel linings: Further insights from full-scale ring tests. Tunnelling and Underground Space Technology, 2018, 79: 304–318
19. Ding W, Gong Y, Qiao Y, Gong C. Experimental investigation on mechanical behavior of segmental joint under combined loading of compression-bending-shear. Tunnelling and Underground Space Technology, 2020, 98: 103346
20. Salemi A, Esmaeili M, Sereshki F. Normal and shear resistance of longitudinal contact surfaces of segmental tunnel linings. International Journal of Rock Mechanics and Mining Sciences, 2015, 77: 328–338
21. Chen R P, Chen S, Wu H N, Liu Y, Meng F Y. Investigation on deformation behavior and failure mechanism of a segmental ring in shield tunnels based on elaborate numerical simulation. Engineering Failure Analysis, 2020, 117: 104960
22. Dong H, Wu Y, Zhao Y, Liu J. Behavior of deformation joints of RC utility tunnels considering multi-hazard conditions. Case Studies in Construction Materials, 2022, 17: e01522
23. Jin Y, Ding W, Yan Z, Soga K, Li Z. Experimental investigation of the nonlinear behavior of segmental joints in a water-conveyance tunnel. Tunnelling and Underground Space Technology, 2017, 68: 153–166
24. Xu Y, Huang Z, Zhang C, Pang Y, Liu T. Bearing capacities and failure behaviors of f-type socket joint in rectangular pipe-jacking tunnel. Applied Sciences, 2023, 13(9): 5442